POLITECNICO DI MILANO

Facoltà di Ingegneria Industriale

Corso di Laurea in
Ingegneria Aeronautica

CFD ANALYSIS OF A NACELLE AT HIGH ANGLE OF INCIDENCE

Relatore: Prof. Alberto Guardone

Tesi di Laurea di:

Jacopo Lucioli Matr. 739998

Anno Accademico 2010 - 2011

Abstract

Nacelles design is a complex process which must fulfill geometrical constraints and engine requirements. A fundamental requirement is the homogeneity of the flow in front of the fan which is quantified by the total pressure distribution in this plane. A critical situation is when the airplane on the ground rotates during the take off with the nacelle at high angle of attack. The risk of the flow separation at the intake is highly probable. Understanding the physics of such flows is a priority, and high fidelity Computational Fluid Dynamics capabilities can be the instrument. CFD solvers provides a cost-effective solutions of the flow field in a reasonable time. It is an accurate alternative to scale model testing, with variations on the simulation being performed quickly, offering obvious advantages. The main aim of the present project is the understanding of the separation phenomenon which take place inside a nacelle at high angle of attack using a numerical approach by solving the Reynolds-averaged Navier-Stokes equations in combination with eddy-viscosity turbulence models. The commercial code CFX, which uses the finite volume method to solve the RANS equations, has been employed. The process of performing a single CFD simulation duly described. The geometry definition with CATIAv5 and the mesh generation with ICEM are presented. Block structured hexahedral mesh has been used due to its high accuracy in solving viscous problem. Simulations for different design configuration and boundary conditions has been carried out for both incompressible and compressible steady flow. At high angle of incidence the flow approaching the nacelle lip decelerates until the stagnation point and then accelerates inside the inlet. The flow detaches under the effect of strong pressure gradient and far inside the nacelle it reattaches generating a separation bubble. This phenomenon generate a heterogeneous total pressure distribution, called distortion. Results show that the distortion is influenced by the mass flow of the nacelle.

Sommario

La progettazione della gondola o nacelle è un processo complesso che deve soddisfare vincoli geometrici e requisiti motoristici. Un requisito fondamentale è l'omogeneità del fluido all'entrata del motore in prossimità della ventola, questa omogeneità è quantificabile dal livello di distorsione del campo di pressione totale in questo piano. Una situazione critica si presenta quando l'aeromobile si trova a terra in fase di decollo, con la nacelle ad un angolo di attacco elevato. Il rischio di separazione del flusso all'ingresso della Nacelle è altamente probabile. Studiare la fisica del flusso d'aria in tale situazione è fondamentale, e lo strumento giusto può essere rappresentato dalla fluidodinamica computazionale (CFD). I risolutori CFD sono in grado di dare soluzioni del campo di moto in maniera efficiente e in tempi ragionevoli. Rappresentano una valida alternativa alle prove su modelli in galleria del vento, soprattuto quando è necessario variare velocemente la configurazione oggetto della prova, offrendo così evidenti vantaggi. Tale tesi ha come principale obiettivo la comprensione del fenomeno della separazione che avviene all'interno della nacelle ad angoli di attacco elevati usando un approccio numerico risolvendo le equazione mediate di Navier-Stokes (RANS) con modelli di turbolenza viscosa k-w SST. Abbiamo utilizzato CFX, un software commerciale che impiega un metodo a volumi finiti per risolvere le RANS. Il proparazione di una generica simulazione CFD è completamente descritta, iniziando dalla definizione del modello geometrico in CATIAv5 e la generazione della griglia di calcolo con ANSYS ICEM. Sono state utilizzate griglie a celle esaedriche definite a blocchi al fine di sfruttare la loro elevata precisione nel risolvere problemi viscosi. Sono state eseguite simulazioni per diverse configurazioni e condizioni al contorno, in flusso incomprimible stazionario e in flusso comprimibile stazionario. Ad elevati angoli di incidenza il flusso che si avvicina al bordo di attacco della nacelle decelera fino al punto di ristagno e successivamente accelera all'interno della presa. Il flusso separa sotto l'effetto di un forte gradiente di pressione ben all'interno della nacelle e riattacca creando una bolla di separazione. Questo fenomeno genera una distribuzione di pressione totale eterogenea, chiamato distorsione, presente sul piano virtuale che rappresenta la ventola. I risultati mostrano che la distorsione è influenzata del flusso di massa che attravera la nacelle.

Contents

List of Figures

List of Tables

Chapter 1

Introduction and motivations

1.1 Introduction

Nacelles design is a complex process in which geometrical constraints as well as engine requirements must be satisfied. A fundamental requirement is the assurance of the homogeneity of the flow in front of the fan which is quantified by the distortion levels of the total pressure in this plane. A critical situation is when the airplane is on the ground, rotating during the take off with a high angle of attack wind on the nacelle. In this situation separations may occur in the inlet, depending on the engine mass flow rate. The study of the effect of flow separations at the intake of a turbo-compressor engine is consequently an important subject of interest for the aeronautic field. Separations generate a distorted distribution of pressure at the entrance of the engine's rotor. When the distortion is not negligible aerodynamic instabilities of the fan blades may take place deteriorating the functionality of the whole engine. In most dangerous situations if the distortion is large enough, the stall of the fan is a concrete possibility. In the upcoming future both civil and military aero engine compression systems will have more complex architectures, therefore gas turbine engines have to be efficient and capable of operating even in distorted inlet conditions. Understanding the physics of such flows is a priority, and high fidelity CFD capabilities can be the instrument. But the investigation of a distorted flow inside turbo-machines is really complex and a proper model must be create. The combination of the incoming flow's asymmetry with rotating blade-rows calls for a time-accurate solution procedure. The time needed to obtain a reliable solution can be extremely long and also the post-processing with the analysis of the results can be complicated.

In this context we present our work, developed at the numerical laboratory of Ecole Polytechnique de Montreal for the NSERC-J.A.Bombardier-Pratt & Whitney Canada in-

dustrial research chair in design integration for more efficient aircraft held by Professor Jean-Yves Trépanier. The main aim of the project is the understanding of the separation phenomenon which take place inside a nacelle at high angle of attack using a numerical approach with Computational Fluid Dynamic simulations. Fast and accurate computations are required by engineers in nacelles design context. Therefore computational predictions for such flows are obtained by solving the Reynolds-averaged Navier-Stokes equations in combination with eddy-viscosity turbulence models.

In particular we will test different geometric configurations and boundary conditions trying to find in which way they influence the separation.

1.2 Thesis outline

Chapter 2 introduces the reader to the conceptual fundaments of CFD and describe the work procedure of the project, from the creation of the geometrical model to the analysis of the results, providing a briefly introduction for each software used during the research.

In Chapter 3 the base equations modeling the flow field, the Navier-Stokes equations for compressible viscous flows, are presented, followed by the turbulence model adopted. Chapter 4 describes the Finite Volume Method implemented in CFX, the numerical method used to discretize and solve the RANS equations.

Chapter 4 describes the meshing procedure, introducing different meshing technique and focusing on the hexahedral block-structured grid generation.

The effective calculations and results analysis are presented in Chapter 5, together with every design step and all the boundary conditions we tested.

Finally Chapter 6 provides conclusions together with some considerations about future studies.

Chapter 2

Numerical simulation in fluid dynamics

For many years computers have been a powerful tool to solve fluid flow problems. From the mid-1970's Computational Fluid Dynamics solvers were developed thanks to the understanding of the complex mathematics required to generalize the algorithms. In 1980's these solvers began to be used but they were not still popular because they needed extremely powerful computer, a large amounts of time to set up simulations.and an in-depth knowledge of fluid dynamics. Nowadays the process of creating a CFD model and analyzing results is less problematic and expensive thanks to much more potent computers, innovate graphics and 3D manipulation tools. CFD solvers provides a cost-effective solutions of the flow field in a reasonable time. It is an accurate alternative to scale model testing, with variations on the simulation being performed quickly, offering obvious advantages. As a result of these factors, CFD now an established industrial design tool, helping to reduce design time scales and improve processes throughout the engineering world.

In this section we are going to briefly introduce to the model of the nacelle we consider in our simulations and to three licensed software we employed in our work: CATIAv5, ICEM and CFX.

2.1 The Nacelle model description

The nacelle is a cover housing (separate from the fuselage) that holds engines, fuel, or equipment on an aircraft. The smooth shape of an aircraft nacelle belies its underlying complexity. While providing an aerodynamic shell for minimum drag, a nacelle also incorporates deicing capability, noise attenuation and mechanisms to reverse engine thrust for

braking. Figure 2.1 shows the basic geometrical model we have used to describe the nacelle under study. As we are going to deepen in chapter 6 we consider just half of a nacelle, in fact we are interested in the investigation of the separation caused by the presence of a large angle of attack, 25°, at a far-field inlet speed of 77m/s, for this reason we assume the solution to be symmetric[1] respect the x-y plane passing through the engine axis. The surface of trailing edge of the nacelle is defined lip, the internal surface going from the lip to the fan is the diffuser. The fan is represented as a semicircular plane. In selected configurations we consider an empty nacelle, with the possibility for the flow to pass through. In others we also represent the covering nose.

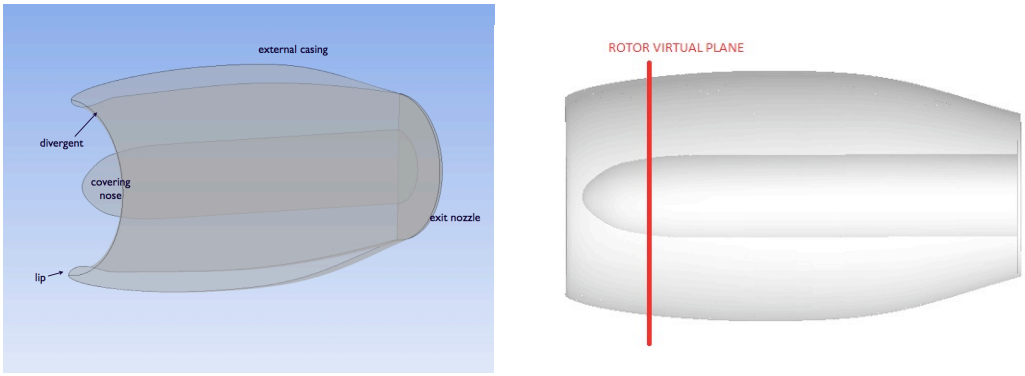

Figure 2.1: Nacelle model

2.2 Preparation of the numerical simulation

The geometry of the component is created with the CAD program CATIAv5. The geometrical model is then imported in a mesh generator software called ICEM. The mesh is then created. CFX is the software we used to numerically simulate our problem. The mesh is imported in its pre-processor ambience, and there we define other elements of the simulation including the boundary conditions and the fluid properties. After that the solver is run to produce the flow solution containing all the variables of the problem calculated in the entire domain. The steady results can be visualized providing an understanding of the behavior of the fluid throughout the region of interest. This can lead to design modifications that can be tested by changing the geometry of the CFD model and seeing the effect.

The process of performing a single CFD simulation is split therefore into four compon-

[1]We assume the trasversal effect are negligeble in the problem under study, even if the time evolution of the separation is never symmetric.

ents:

1. Creating the geometry
2. Creating the mesh
3. Defining the physics of the model and solving the CFD problem
4. Visualizing the results in the post-processor

These steps are described in details in the following.

2.2.1 Creation of the geometric model with CATIAv5

The geometric model of our nacelle is created with CATIAv5 a commercial CAD (Computer-Aided Design) software extensively used in aerospace industries.

CAD is mainly used for detailed engineering of 3D models but it is also used throughout the engineering process from conceptual design with benefits such as lower product development costs and a greatly shortened design cycle.

We approximate the nacelle as a solid generated from a 180° revolution of a generic airfoil around the symmetry axis. Once the basic geometric model is complete we import it into ICEM, a meshing software we are going to describe better in the next section. Utilizing the geometrical tools of ICEM we complete the nacelle structure adding specific part as fan surface and covering nose or particular rear configurations. Finally we build the external box which contains the nacelle and represent the calculation domain.

2.2.2 Creation of the mesh with ICEM

ANSYS ICEM CFD is a meshing generation software. It is composed by effecient tools for repairing and modifing imported CAD/geometry and it provides a large variety of meshing techniques. It is particularly useful for our project thanks to the advanced control on hexahedral block-structured mesh with an extended mesh diagnostics. Once the geometrical domain is completely defined we starts the meshing procedure consisting in dividing the field in blocks and meshing each of them utilizing hexahedral elements.

2.2.3 Numerical simulation with CFX

The set of equations that enforce the conservation of mass and the balance of momentum and total energy are known as the Navier-Stokes equations. These partial differential equations were derived in the early nineteenth century and have no known general analytical

solution but can be discretized and solved numerically. There are a number of different solution methods that are used in CFD codes. The one on which CFX is based, is known as the finite volume technique. In this technique, the region of interest is divided into small sub-regions, called control volumes.The equations are discretized and solved iteratively for each control volume. As a result, an approximation of the value of each variable at specific points throughout the domain can be obtained.

ANSYS CFX consists of four software modules which take a geometry and mesh and pass the information required to perform a CFD analysis, as depicted in figure 2.2.

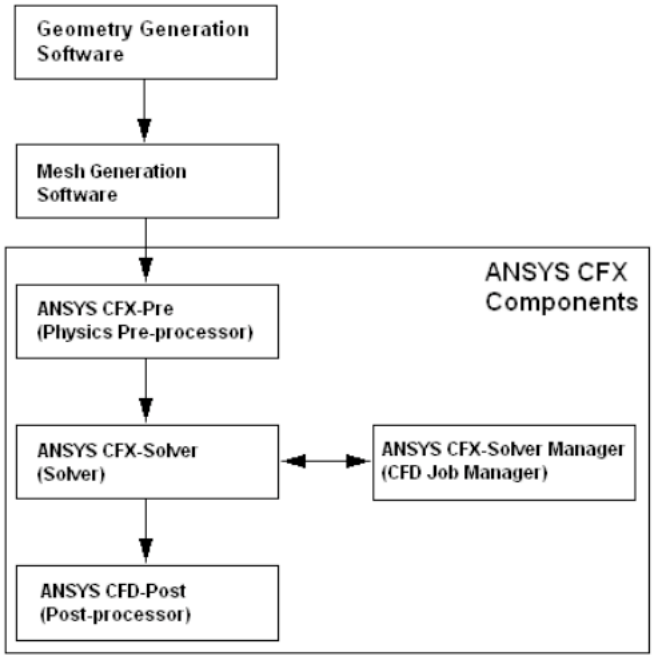

Figure 2.2: CFX modules scheme

All CFX codes contain three main elements:

A pre-processor, which is used to define the flow properties, the solution model, the boundary conditions and the solver parameters.

A flow solver, which is used to solve the governing equations of the flow subject to the conditions provided. It produces the required results in a non-interactive/batch process. A CFD problem is solved as follows:

1. The partial differential equations are integrated over all the control volumes in the

region of interest. This is equivalent to applying a basic conservation law to each control volume.

2. The integral equations are converted into a system of algebraic equations by generating a set of approximations for the terms in the integral equations.

3. The algebraic equations are solved iteratively.

An iterative approach is required because of the non-linear nature of the equations, and as the solution approaches the exact solution, it is said to converge. For each iteration, an error, or residual, is reported as a measure of the overall conservation of the flow properties. How close the final solution is to the exact solution depends on a number of factors, including the size and shape of the control volumes and the size of the final residuals. Turbulence are modeled using empirical relationships. The solution process requires no user interaction and is, therefore, usually carried out as a batch process. The solver produces a results file that is then passed to the post-processor.

A post-processor, which is used to organize the data and show the results in graphical and easy to read format. We employ it in particular for visualization of the geometry and control volume , contour plots showing magnitude of the flow properties, visualizations of the variation of scalar variables through the domain and quantitative numerical calculations.

Chapter 3

The mathematical model for high-Reynolds compressible viscous flows

This chapter describes the mathematical equations used to model the fluid , heat, and mass transfer for single-phase, single-component compressible viscous flow. In order to accurately simulate the hydrodynamic flows , the model must account for turbulence. We will present the Navier Stokes equations, as well as their Reynolds-avarege form which are effectively implemented in CFX. Then the $k - w$ SST (shear stress transport) turbulence model is described.

3.1 The Navier-Stokes equations

The Navier-Stokes equations in their conservation form describe the behavior of a viscous compressible flow. The instantaneous equations of mass, momentum and energy conservation can be written as follows in a stationary frame:

$$\frac{\partial \rho}{\partial t} + \nabla \bullet (\rho U) = 0 \tag{3.1}$$

$$\frac{\partial (\rho U)}{\partial t} + \nabla \bullet (\rho U \otimes U) = \nabla p + \nabla \bullet \tau + \rho \mathbf{g} \tag{3.2}$$

$$\frac{\partial \rho h_{tot}}{\partial t} - \frac{\partial p}{\partial t} + \nabla \bullet (\rho U h_{tot}) = \nabla \bullet (\lambda \nabla T) + \nabla \bullet (U \bullet \tau) + U \bullet \rho \mathbf{g} \tag{3.3}$$

where the stress tensor, τ, is related to the velocity by

$$\tau = \mu(\nabla U + (\nabla U)^T - \frac{2}{3}\delta \nabla \bullet U) \tag{3.4}$$

where ρ is the density, p the pressure, U is the velocity vector, t is time, μ is the dynamic viscosity, g is the gravity vector, λ is the thermal conductivity , h_{tot} is defined as the specific total enthalpy, which for the general case of variable properties and compressible flow is given in terms of the specific static (thermodynamic) enthalpy, h, by:

$$h_{tot} = h + \frac{1}{2}U^2 \tag{3.5}$$

where

$$h = h(p, T)$$

There are seven unknowns (u, v, w, p, T, ρ, h) in the above five equations. The set can be closed by adding two algebraic thermodynamic equations: the Equation of State, which relates density to pressure and temperature; and the Constitutive Equation, which relates enthalpy to temperature and pressure.

Equation of state

The thermal equation of state is described as a function of both temperature and pressure:

$$\rho = \rho(p, T) \tag{3.6}$$

The specific heat capacity, C_p, may also be described as a function of temperature and pressure:

$$C_p = C_p(p, T) \tag{3.7}$$

We are going to consider ideal gas with density defined by the ideal gas law (eq. 3.8) and constant C_p .

$$\rho = \frac{w(p + p_{ref})}{R_0 T} \tag{3.8}$$

where w is the molecular weight of the gas, and R_0 is the universal gas constant.

Constitutive equation

The constitutive equation is a thermodynamic equation of state for enthalpy as a function of both temperature and pressure. For ideal with constant specific heat we define the enthalpy change by:

$$h_{stat} - h_{ref} = C_p(T_{stat} - T_{ref}) \tag{3.9}$$

3.1.1 Boundary conditions

The equations relating to fluid flow can be closed by the specification of conditions on the external boundaries of a domain. It is the boundary conditions that produce different solutions for a given geometry and set of physical models. Hence, the problem solution deeply depends on the assigned boundary conditions. Therefore, it is important to set boundary conditions that accurately reflect the real situation to allow you to obtain accurate results.

Boundary conditions are a set of properties or conditions on surfaces of domains, and are required to fully define the flow simulation. The type of boundary condition that can be set depends upon the bounding surface.

The problem is well-posed, if suitable boundary and initial condition are given. These are going to be discussed in section 6.1 .

3.1.2 Turbulence model

Turbulence involves fluctuations in the flow field both in time and space, it is a complex three dimensional, unsteady process which consists of many scales. It can deeply affect the flow characteristics. Turbulence it occurs when the inertial forces in the fluid become considerable when compared to viscous forces. Navier-Stokes equations describe both laminar and turbulent flows, but turbulent flows at realistic Reynolds Numbers cover a wide range of time scales and turbulent length and could easily involve length scales smaller than the smallest finite volume mesh which can be conveniently used in a numerical analysis. Therefore the Direct Numerical Simulation (DNS) of such flows would require a computing

power many orders of magnitude higher than the one available in the foreseeable future. A considerable amount of CFD research focused on developing methods which use turbulence models in order to consider and predict the effects of turbulence thus avoiding the use of a prohibitively fine mesh and Direct Numerical Simulation. Large Eddy Simulation (LES) and Reynolds Average Navier-Stokes (RANS) are the main methods adopted. The LES approach consists in the application of a spacial filter which separates the big scales, solved with the Navier-Stokes equations, and the small scales of the turbulent field.The small turbulent scales are modeled considering them homogeneous and isotropic. The finer is the mesh the closer the LES solutions are to the DNS ones, but this technique is still really expensive and for this reason RANS approach, which is going to be introduced in next sub-section, is still the most commonly adopted.

3.1.2.1 RANS equations

When considering time scales larger that the turbulent fluctuations ones, turbulent flow can be represented by average charateristics while adding a time-varying fluctuating component. For example a velocity component may be divided into an average and a time varying component. Generally turbulence models introduce averaged and fluctuating quantities in order to modify the original unsteady Navier-Stokes equations and produce the Reynolds averaged Navier-Stokes equations. These equations represent the mean flow quantities and model turbulence effects without the need to solve the turbulent fluctuations. All scales of the turbulence field are modeled.

RANS equations based models are known as Statistical Turbulence Models, the name is due to the statical averaging procedure used to obtain the equations. The computational effort required by the simulation of the RANS equations is much smaller than the one required by Direct Numerical Simulation, so these simulations are preferred for practical engineering calculations. A consequence of the averaging procedure is the introduction of further unknown terms which contain products of the fluctuating quantities: these therms, difficult to determine directly, act like additional stresses within the fluid and are named 'turbulent' or Reynolds' stresses. In order to achieve closure of the equations system Reynolds stresses are to be modeled by further equations involving known quantities. The type of turbulence model is defined by the equations employed to close the system.

The RANS approach relies on the idea of separating every variables (general variable ψ) in two components, an average part $\overline{\psi}$ and a fluctuating part ψ'.

$$\psi = \overline{\psi} + \psi' \tag{3.10}$$

the average part is given by:

$$\overline{\psi} = \lim_{T\to\infty} \frac{1}{T} \int_0^T \psi dt \tag{3.11}$$

Applying this decomposition at the Navier-Stokes equations 3.12and3.17and3.14, we obtain te Raynolds-averaged equations :

$$\frac{\partial \bar{\rho}}{\partial t} + \nabla \bullet (\bar{\rho}\bar{U}) = 0 \tag{3.12}$$

$$\frac{\partial (\bar{\rho}\bar{U})}{\partial t} + \nabla \bullet (\bar{\rho}\bar{U} \otimes \bar{U}) = -\nabla \bar{p} + \nabla \bullet (\bar{\tau} - \bar{\rho}\overline{U' \otimes U'}) + \bar{\rho}\mathbf{g} \tag{3.13}$$

$$\frac{\partial \bar{\rho}\bar{h}_{tot}}{\partial t} - \frac{\partial \bar{p}}{\partial t} + \nabla \bullet (\bar{\rho}\bar{U}\bar{h}_{tot}) = \nabla \bullet (\lambda \nabla \bar{T} - \bar{\rho}\overline{U'h}) + \nabla \bullet (\bar{U} \bullet (\bar{\tau} - \bar{\rho}\overline{U' \otimes U'}) \tag{3.14}$$

As we can see the continuity equation 3.12has not be altered and is similar to3.1. While the momentum and energy equation has been modified.

The term $\overline{\rho U' \otimes U'}$ is the Reynold stress tensor. This term is generated by the non-linear convective term in the un-averaged equations. Turbulent velocity fluctuations give rise to turbulent convective transport, thus increasing the mixing effect at molecular level generally created by thermal fluctuations. At high Reynolds numbers turbulent velocity fluctuations take place over a length scale much larger than the thermal fluctuations mean free path resulting in turbulent fluxes being much larger than molecular fluxes.

The average total enthalpy is given by:

$$\bar{h}_{tot} = h + \frac{1}{2}\bar{U}^2 + k \tag{3.15}$$

where k is the turbulent kinetic energy:

$$k = \frac{1}{2}\overline{U'^2} \tag{3.16}$$

The Reynolds stress tensor needs to be modeled in order to close the problem. We presents two approaches to solve this problem. A first way can be modelling the Reynolds stress tensor using specific transport equations. The second method is the eddy viscosity model, it is the approach we are going to utilize and it will be described in the next subsection.

3.1.2.2 Eddy viscosity turbulence model

The eddy viscosity turbulence model is based on the Boussinesq's hypothesis which assumes that the turbulent stress tensor can be expressed as a linear function of the strain rate tensor, in analogy with relationship between the stress and strain tensors in laminar Newtonian flow:

$$-\bar{\rho}\overline{U' \otimes U'} = -\frac{2}{3}\delta(\bar{\rho}k + \mu_t \nabla \bullet U) + \mu_t(\nabla \bar{U} + (\nabla \bar{U})^T)) \tag{3.17}$$

where μ_t is the turbulent eddy viscosity and has to be modeled.
The Reynolds averaged momentum and scalar transport equations become:

$$\frac{\partial(\bar{\rho}\bar{U})}{\partial t} + \nabla \bullet (\bar{\rho}\bar{U} \otimes \bar{U}) = -\nabla p' + \nabla \bullet (\mu_{eff}(\nabla \bar{U} + (\nabla \bar{U})^T)) + \bar{\rho}\mathbf{g} \tag{3.18}$$

where μ_{eff} is the Effective viscosity defined by:

$$\mu_{eff} = \mu + \mu_t \tag{3.19}$$

and p' is the modified pressure, defined by:

$$p' = \bar{p} + \frac{2}{3}(\bar{\rho}k + \mu_t \nabla \bullet U) \tag{3.20}$$

The problem is now the determination of μ_t for which different models exist:

- zero-equations models, where no additional transport equations are solved and an algebraic equation is used to calculate the viscous contribution from turbulent eddies (Prandtl's mixing length model).
- one-equations models, (Spalart-Allmaras model).
- two-equations models, where both the velocity and length turbulent scale are solved using separate transport equations ($k - \epsilon$ and $k - \omega$ models).

We adopted a specific variation of a $k - \omega$ two-equations model: the $k - \omega$ SST.

The $k - w$ *Shear Stress Transport* model

The generic $k - \omega$ two-equation model use the gradient diffusion hypothesis to relate the Reynolds stresses to the mean velocity gradients and the turbulent viscosity. The turbulent viscosity is modeled as the product of a turbulent velocity and turbulent length scale. In two-equation models the turbulence velocity scale is computed from the turbulent kinetic

energy, which is provided from the solution of its transport equation. The turbulent length scale is estimated from two properties of the turbulence field, usually the turbulent kinetic energy and its dissipation rate. The dissipation rate of the turbulent kinetic energy is obtained from the solution of its transport equation.

One of the main problems in turbulence modeling is the accurate prediction of flow separation from a smooth surface. Standard two-equation turbulence models often fail to predict the onset and the amount of flow separation under adverse pressure gradient conditions. This is the most important phenomenon that we want to analyze in the present work. For this reason, we are going to use an advanced turbulence models for this application. In general, turbulence models based on the equation predict the onset of separation too late and under-predict the amount of separation later on. The prediction is therefore not on the conservative side from an engineering stand-point. The models developed to solve this problem have shown a significantly more accurate prediction of separation in a number of test cases and in industrial applications.

Currently, the most prominent two-equation models in this area are the $k - w\ SST$ based models of Menter [11].

It was designed to give a highly accurate predictions of the onset and the amount of flow separation under adverse pressure gradients by the inclusion of transport effects into the formulation of the eddy-viscosity. This results in a major improvement in terms of flow separation predictions. The good performance of this model has been demonstrated in a large number of validation studies (Colin [12]) .

The SST model is recommended for high accuracy boundary layer simulations. To benefit from this model, a resolution of the boundary layer of more than 10 points is required.

$$\frac{\partial(\bar{\rho}k)}{\partial t} + \nabla \bullet (\bar{\rho}\bar{U}k) = \nabla \bullet \left[\left(\mu + \frac{\mu_t}{\sigma_{k3}}\right)\nabla k\right] + P_k - \beta'\bar{\rho}k\omega \tag{3.21}$$

$$\frac{\partial(\bar{\rho}\omega)}{\partial t} + \nabla \bullet (\bar{\rho}\bar{U}\omega) = \nabla \bullet \left[\left(\mu + \frac{\mu_t}{\sigma_{\omega 3}}\right)\nabla\omega\right] + 2(1-F_1)\bar{\rho}\frac{1}{\sigma_{\omega 2}\omega} + \alpha_3\frac{\omega}{k}P_k - \beta_3\bar{\rho}\omega^2 \tag{3.22}$$

wher the production term P_k is given by :

$$P_k = \min\left(\tau\nabla\bar{U},\ 10\beta^* k\omega\right) \tag{3.23}$$

The kinematic eddy viscosity ν_t is given by:

$$\nu_t = \frac{\alpha_1 k}{\max(\alpha_1 \omega,\ SF_2)} \tag{3.24}$$

where

$$\nu_t = \frac{\mu_t}{\bar{\rho}} \tag{3.25}$$

The interface function F_1 and F_2 formulation is based on the distance to the nearest surface and on the flow variables.

$$F_1 = tanh(arg_1^4) \tag{3.26}$$

$$arg_1 = \min\left(\max\left(\frac{\sqrt{k}}{\beta'\omega y},\ \frac{500\mu}{y^2\omega\bar{\rho}}\right),\ \frac{4\bar{\rho}k}{CD_{kw}\sigma_{\omega 2}y^2}\right) \tag{3.27}$$

where y is the distance to the nearest wall and $CD_{k\omega}$ is a redistributive term.

$$CD_{k\omega} = \max\left(2\bar{\rho}\frac{1}{\sigma_{\omega 2}\omega}\nabla k\nabla\omega,\ 10^{-10}\right) \tag{3.28}$$

$$F_2 = tanh(arg_2^2) \tag{3.29}$$

$$arg_2 = \max\left(\frac{2\sqrt{k}}{\beta'\omega y},\ \frac{500\nu}{y^2\omega}\right) \tag{3.30}$$

Initial and boundary conditions are generally imposed as a fixed value, given by the empirical formulas:

$$k = \frac{3}{2}(U_{inf}I)^2 \qquad\qquad \omega = C_\mu^{-\frac{1}{4}}\frac{\sqrt{k}}{l} \tag{3.31}$$

where U_{inf} is the free-stream velocity modulus, I is the free-stream turbulence intensity, C_μ is a constant which has a value of 0.009 and l is the turbulent length-scale.

All coefficients are listed again for completeness:

$$\beta' = 0.09$$

$$\alpha_1 = 5/9 \qquad \beta_1 = 0.075 \qquad \sigma_{k1} = 2 \qquad \sigma_{\omega 1} = 2$$

$$\alpha_2 = 0.44 \qquad \beta_2 = 0.0828 \qquad \sigma_{k2} = 1 \qquad \sigma_{\omega 2} = 1/0.856$$

The coefficients with subscri 3 are a linear combination of the corresponding coefficients 1 and 2:

$$\Phi_3 = F_1 \Phi_1 + (1 - F_1)\Phi_2$$

Chapter 4

Numerical discretization and solution of the compressible flow equations

Solve exactly the Navier-Stokes equations for real flows is not feasible hence a numerical approach must be adopted. In order to simplify the problem and obtain a solution the differential equations are replaced by algebraic approximations obtained from a discretization procedure. In general this procedure is composed by two parts: the time and space domain discretization and equation discretization. The spatial domain is divided into discrete parts (points, surfaces, volumes) over which the governing equations are integrated after they have been transformed into algebraic expressions. In this chapter we are goimg to present the numerical technique implemented in the solver CFX.

4.1 Finite volume method

To approximate the flow equations in space CFX adopts the Finite Volume Method. This technique involves discretising the spatial domain into finite control volumes using a mesh. The governing equations in an integral form are discretized and solved over each control volume, such that the relevant quantity (mass, momentum, energy etc.) is conserved in a discrete sense for each control volume.

Figure 4.1 shows a typical control volume. Each control volume must not overlap with others and the composition all the volumes must cover the whole domain. To each volume is associated his centroid P where the solution is calculated and certain number of flat faces defined by a face area vector S. Each face can compose the external surface of the domain if it is a boundary face or it can be shared with another volume (with centroid N).

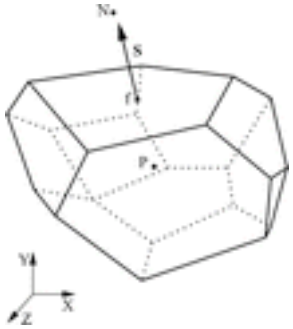

Figure 4.1: discrete volume

It is clear that each node is surrounded by a set of surfaces which comprise the finite volume. All the solution variables and fluid properties are stored at the element nodes. Consider the mean form of the conservation equations for mass, momentum and a passive scalar, expressed in cartesian coordinates:

$$\frac{\partial \rho}{\partial t} + \frac{\partial}{\partial x_j}(\rho U_j) = 0 \tag{4.1}$$

$$\frac{\partial}{\partial t}(\rho U_i) + \frac{\partial}{\partial x_j}(\rho U_j U_i) = -\frac{\partial P}{\partial x_i} + \frac{\partial}{\partial x_j}\left(\mu_{eff}\left(\frac{\partial U_i}{\partial x_j} + \frac{\partial U_j}{\partial x_i}\right)\right) \tag{4.2}$$

$$\frac{\partial}{\partial t}(\rho \phi) + \frac{\partial}{\partial x_j}(\rho U_j \phi) = \frac{\partial}{\partial x_j}\left(\Gamma_{eff}\left(\frac{\partial \phi}{\partial x_j}\right)\right) + S_\phi \tag{4.3}$$

These equations are integrated over a control volume, and Gauss divergence theorem is applied to convert some volume integrals to surface integrals. For control volumes that do not deform in time, the time derivatives can be moved outside of the volume integrals and the equations become:

$$\frac{d}{dt}\int_V \rho dV + \int_V \rho U_j dn_j = 0 \tag{4.4}$$

$$\frac{d}{dt}\int_V \rho U_i dV + \int_s \rho U_j U_i dn_j = -\int_s P dn_j + \int_s \mu_{eff}\left(\frac{\partial U_i}{\partial x_j} + \frac{\partial U_j}{\partial x_i}\right) dn_j \tag{4.5}$$

$$\frac{d}{dt}\int_V \rho \phi dV + \int_s \rho U_j \phi dn_j = \int_s \Gamma_{eff}\left(\frac{\partial \phi}{\partial x_j}\right) dn_j + \int_V S_\phi dV \tag{4.6}$$

where V and s respectively denote volume and surface regions of integration, and dn_j are the differential Cartesian components of the outward normal surface vector. The surface

integrals are the integral of the fluxes, whereas the volume integrals represent source or accumulation terms.

This method works by converting volume integrals to surface integrals (divergence theorem) which can be evaluated as fluxes at the cell walls. The flux entering each cell must equal the flux leaving through the walls which makes the method conservative. On structured meshes it is easily parallelized, as each cell only needs information from neighboring cells and the order is predeterrmined.

The first step in solving these continuous equations numerically is to discretize the volume and surface integrals. Figure 4.2 shows an isolated mesh element.

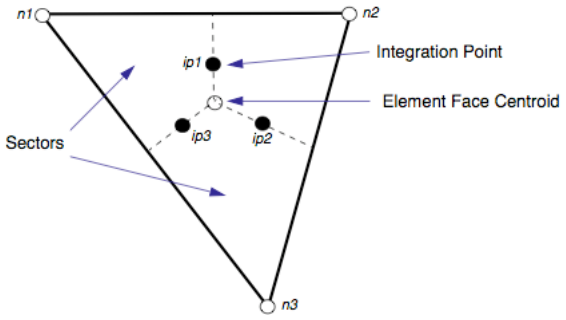

Figure 4.2: mesh element

The surface fluxes must be discretely represented at the integration points to complete the conversion of the continuous equation into their discrete form. The integration points, *ipn*, are located at the centre of each surface segment in a 3D element surrounding the finite volume.

The discrete form of the integral equations are written as:

$$V\left(\frac{\rho-\rho^o}{\triangle t}\right)+\sum_{ip}\left(\rho U_j\Delta n_j\right)_{ip}=0 \tag{4.7}$$

$$V\left(\frac{\rho U_i-\rho^o U_i^o}{\triangle t}\right)+\sum_{ip}\dot{m}_{ip}\left(U_i\right)_{ip}=\sum_{ip}\left(P\Delta n_i\right)_{ip}+\sum_{ip}\left(\mu_{eff}\left(\frac{\partial U_i}{\partial x_j}+\frac{\partial U_j}{\partial x_i}\right)\Delta n_j\right)_{ip} \tag{4.8}$$

$$V\left(\frac{\rho\phi-\rho^o\phi^o}{\triangle t}\right)+\sum_{ip}\dot{m}_{ip}\phi_{ip}=\sum_{ip}\left(\Gamma_{eff}\frac{\partial\phi}{\partial x_j}\Delta n_j\right)_{ip}+\overline{S_\phi}V \tag{4.9}$$

where V is the control volume, the subscript ip denotes an integration point, the

summation is over all the integration points of the finite volume, Δn_j is the discrete outward surface vector, Δt is the timestep. To approximate the time derivative the First Order Backward Euler scheme has been used. Superscripts o refers to the old time level. The discrete mass flow through a surface of the finite volume is denoted by $\dot{m}_{ip}$ and is given by:

$$\dot{m}_{ip} = (\rho U_j \triangle n_j)^o_{ip} \tag{4.10}$$

This expression must be discretized carefully to lead to proper pressure-velocity coupling and to accurately handle the effects of compressibility, as discussed below.

4.1.1 Pressure-Velocity coupling

CFX uses a single cell, unstaggered, collocated grid to overcome the decoupling of pressure and/or velocity in incompressible flows. By applying a momentum-like equation to each integration point, the following expression for the advecting (mass-carrying) velocity at each integration point is obtained:

$$U_{i,ip} = \bar{U}_{i,ip} + f_{ip}\left(\left.\frac{\partial p}{\partial x_i}\right|_{ip} - \left.\frac{\bar{\partial p}}{\partial x_i}\right|_{ip}\right) - c_{ip} f_{ip}\left(U^o_{i,ip} - \bar{U}^o_{i,ip}\right) \tag{4.11}$$

where:

$$f_{ip} = \frac{d_{ip}}{1 - c_{ip} d_{ip}} \tag{4.12}$$

$$d_{ip} = -\frac{V}{A} \tag{4.13}$$

A=approximation to the central coefficient of momentum of momentum equation, excluding the transient term

$$c_{ip} = \frac{\rho}{\Delta t} \tag{4.14}$$

The overbars indicate averaging of adjacent vertex values to the integration point.

The discretization, given simply by averaging the adjacent vertex velocities to the integration point, is augmented by a high-order pressure variation that scales with the mesh spacing. The continuity equation is a second order central difference approximation to the first order derivative in velocity, modified by a fourth derivative in pressure which acts to redistribute the influence of the pressure. This overcomes the problem of checker

board oscillations which are found when the variables are collocated.

In particular, when substituted into the continuity equation, the term

$$f_{ip}\left(\left.\frac{\partial p}{\partial x_i}\right|_{ip} - \left.\frac{\bar{\partial p}}{\partial x_i}\right|_{ip}\right) \tag{4.15}$$

becomes a fourth derivative of pressure that goes to zero at the rate of $\triangle x^3$ relative to the velocity derivative, so that the desired differential form of continuity is quickly recovered.

4.1.2 Compressibility

A product of the density and the advecting velocity is involved in the definition of mass flow terms in the mass conservation equation. Using Newton-Raphson linearization the discretization of this product is made implicit for compressible flows, :

$$(\rho U)^n \approx \rho^n U^o A + \rho^o U^n A - \rho^o U^o A \tag{4.16}$$

the superscripts n indicate the current iterates. The value of ρ^n is linearized in terms of pressure as

$$\rho^n = \rho^o + \left.\frac{\partial \rho}{\partial p}\right|_T (p^n - p^o) \tag{4.17}$$

4.1.3 Transient term

The First Order Backward Euler scheme approximates the transient term as

$$\frac{\partial}{\partial t}\left(\int_V \rho\phi dv\right) = \rho V\left(\frac{\phi - \phi^o}{\Delta t}\right) \tag{4.18}$$

It is robust, fully implicit, bounded, conservative in time, and does not create a timestep limitation for linear problems. This discretization is, however, only first-order accurate in time and will introduce discretization errors that tend to diffuse steep temporal gradients.

The Second Order Backward Euler scheme approximates the transient term as

$$\frac{\partial}{\partial t}\left(\int_V \rho\phi dv\right) = \frac{\rho V}{\Delta t}\left(\frac{3}{2}\phi - 2\phi^o + \frac{1}{2}\phi^{oo}\right) \tag{4.19}$$

where ϕ^{oo} represents the solution field from the time step before the old time level. This scheme is also robust, implicit, conservative in time, and does not create a time step

limitation. It is also second-order accurate in time, but is not bounded and may hence create some nonphysical overshoots or undershoots in the solution.

4.1.4 Shape functions

The solution fields are stored at the mesh nodes. However, to evaluate many of the terms, the solution field or solution gradients must be approximated at integration points. Finite element linear shape functions has been used to calculate the solution variation within an element.

A variable ϕ varies within an element as follows:

$$\phi = \sum_{i=1}^{Nnode} N_i \phi_i \tag{4.20}$$

where N_i is the shape function for node i and ϕ_i is the value of ϕ at node i. The summation is over all nodes of an element. Shape functions include useful properties such as:

$$\sum_{i=1}^{Nnode} N_i = 1 \tag{4.21}$$

$$At\ node\ j,\ \ N_i = \begin{cases} 1 & i = j \\ 0 & i \neq j \end{cases} \tag{4.22}$$

In CFX are implemented shape function which are linear in terms of parametric coordinates. For the following hexahedral element:

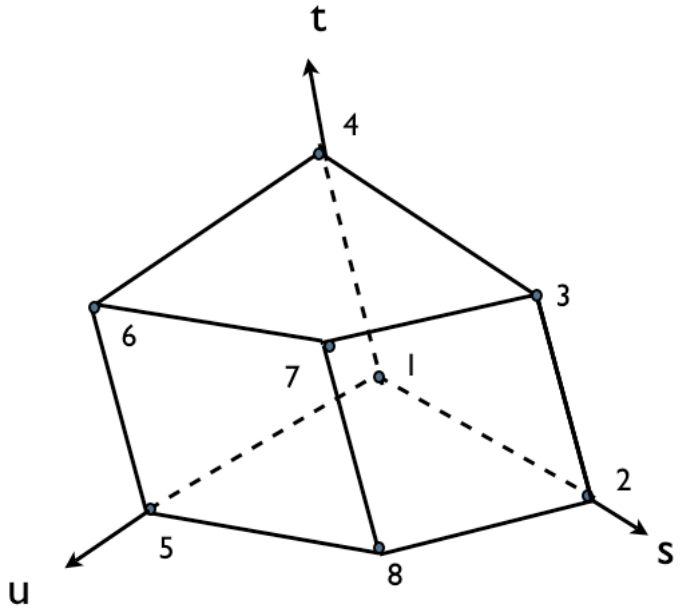

Figure 4.3: hexahedral element

The tri-linear shape functions for each node are

$$N_1(s,t,u) = (1-s)(1-t)(1-u)$$

$$N_2(s,t,u) = s(1-t)(1-u)$$

$$N_3(s,t,u) = st(1-u)$$

$$N_4(s,t,u) = (1-s)t(1-u)$$

$$N_5(s,t,u) = (1-s)(1-t)u$$

$$N_6(s,t,u) = s(1-t)u$$

$$N_7(s,t,u) = stu$$

$$N_8(s,t,u) = (1-s)tu$$

The shape functions are also used to calculate various geometric quantities, such as *ip* coordinates, surface area vectors etc. This is possible because 4.20 holds also for the coordinates:

$$x = \sum_{i=1}^{Nnode} N_i x_i \qquad y = \sum_{i=1}^{Nnode} N_i y_i \qquad z = \sum_{i=1}^{Nnode} N_i z_i$$

4.1.5 Diffusion terms

Following the standard finite element approach, shape functions are used to evaluate the derivatives for all the diffusion terms. For example, for a derivative in the x direction at integration point *ip*,

$$\left.\frac{\partial \phi}{\partial x}\right|_{ip} = \sum_n \left.\frac{\partial N_n}{\partial x}\right|_{ip} \phi_n \tag{4.23}$$

The summation is over all the shape functions for the element. The Cartesian derivatives of the shape functions can be expressed in terms of their local derivatives via the Jacobian transformation matrix:

$$\begin{bmatrix} \frac{\partial N}{\partial x} \\ \frac{\partial N}{\partial x} \\ \frac{\partial N}{\partial x} \end{bmatrix} = \begin{bmatrix} \frac{\partial x}{\partial s} & \frac{\partial y}{\partial s} & \frac{\partial z}{\partial s} \\ \frac{\partial x}{\partial t} & \frac{\partial y}{\partial t} & \frac{\partial z}{\partial t} \\ \frac{\partial x}{\partial u} & \frac{\partial y}{\partial u} & \frac{\partial z}{\partial u} \end{bmatrix}^{-1} \begin{bmatrix} \frac{\partial N}{\partial s} \\ \frac{\partial N}{\partial t} \\ \frac{\partial N}{\partial u} \end{bmatrix} \tag{4.24}$$

The shape function gradients can be evaluated at the actual location of each integration point (true tri-linear interpolation), or at the location where each *ip* surface intersects the element edge (linear-linear interpolation).

4.1.6 Pressure gradient term

The surface integration of the pressure gradient in the momentum equations involves evaluation of the expression:

$$(P \Delta n_{ip})_{ip} \tag{4.25}$$

The value of P_{ip} is evaluated using the shape functions:

$$P_{ip} = \sum_n N_n(s_{ip},\, t_{ip},\, u_{ip}) P_n \tag{4.26}$$

As with the diffusion terms, the shape function used to interpolate P can be evaluated at the actual location of each integration point (true tri-linear interpolation), or at the

location where each *ip* surface intersects the element edge (linear-linear interpolation).

4.1.7 Advection term

The advection term requires the integration point values of ϕ to be approximated in terms of the nodal values of ϕ. The advection schemes implemented can be cast in the form:

$$\phi_{ip} = \phi_{up} + \beta \nabla\phi \bullet \Delta\hat{r} \tag{4.27}$$

where ϕ_{up} is the value at the upwind node, is the gradient of ϕ and $\hat{r}$ is the vector from the upwind node to the *ip*. Particular choices for β give rise to different schemes.

1st Order Upwind Differencing Scheme A value of $\beta = 0$ in eq 4.27 leads to the first order Upwind Difference Scheme (UDS). Many difference schemes developed for CFD are based on series expansion approximations (such as the Taylor series) for continuous functions. The more terms of the expansion used in the difference scheme, the more accurate the approximation will be (but at the expense of increased computational load). The order of the scheme used is denoted by the order of the largest term in the truncated part of the series expansion.

UDS is very robust (numerically stable) and is guaranteed to not introduce non-physical overshoots and undershoots. However, it is also susceptible to a phenomenon known as numerical diffusion.

High resolution scheme The High Resolution Scheme computes β locally to be as close to 1 as possible without violating boundedness principles. The high resolution scheme is therefore both accurate (reducing to first order near discontinuities and in the free stream where the solution has little variation) and bounded.

4.2 The Coupled System of Equations

The linear set of equations that arise by applying the Finite Volume Method to all elements in the domain are discrete conservation equations. The system of equations can be written in the form:

$$\sum_{nb_i} a_i^{nb} \phi_i = b_i$$

where ϕ is the solution, b the right hand side, a the coefficients of the equation, i is the identifying number of the finite volume or node in question, and nb means "neighbour", but also includes the central coefficient multiplying the solution at the ith location. The node may have any number of such neighbours, so that the method is equally applicable to both structured and unstructured meshes. The set of these, for all finite volumes constitutes the whole linear equation system. For a scalar equation (e.g. enthalpy or turbulent kinetic energy), each a_i^{nb}, ϕ_{nb} and b_i is a single number. For the coupled, 3D mass-momentum equation set they are a (4 x 4) matrix or a (4 x 1) vector, which can be expressed as

$$a_i^{nb} = \begin{bmatrix} a_{uu} & a_{uv} & a_{uw} & a_{up} \\ a_{vu} & a_{vv} & a_{vw} & a_{vp} \\ a_{wu} & a_{wv} & a_{ww} & a_{wp} \\ a_{pu} & a_{pv} & a_{pw} & a_{pp} \end{bmatrix}_1^{nb}$$

and

$$\phi_i = \begin{bmatrix} u \\ v \\ w \\ p \end{bmatrix}_i \qquad b_i = \begin{bmatrix} b_u \\ b_v \\ b_w \\ b_p \end{bmatrix}_i$$

It is at the equation level that the coupling in question is retained and at no point are any of the rows of the matrix treated any differently. The advantages of such a coupled treatment over a non-coupled or segregated approach are several: robustness, efficiency, generality and simplicity. These advantages all combine to make the coupled solver an extremely powerful feature of any CFD code. The principal drawback is the high storage needed for all the coefficients.

4.2.1 Solution strategy

The momentum equations are first solved, using a guessed pressure, and an equation for a pressure correction is obtained. This is the solution strategy employed by segregated solvers. A large number of iterations are typically required because of the 'guess-and-correct' nature of the linear system. Also selecting relaxation parameters for the variables is fundamental. CFX uses a coupled solver, which solves the hydrodynamic equations (for u, v, w, p) as a single system. This solution approach uses a fully implicit discretisation of the equations at any given time step. For steady state problems the time-step behaves like an 'acceleration parameter', to guide the approximate solutions in a physically based manner to a steady-state solution reducing the number of iterations riquired for convergence.

4.2.1.1 General solution

The general solution procedure is shown in figure 4.4. The solution of each set of equations shown in the flow chart consists of two numerically intensive operations. For each timestep:

1. The non-linear equations are linearised and assembled into the solution matrix.
2. The linear equations are solved.

The timestep iteration is controlled by the physical timestep (global) or local timestep factor (local) setting to advance the solution in time for a steady state simulation. In this case, there is only one linearisation iteration per timestep.

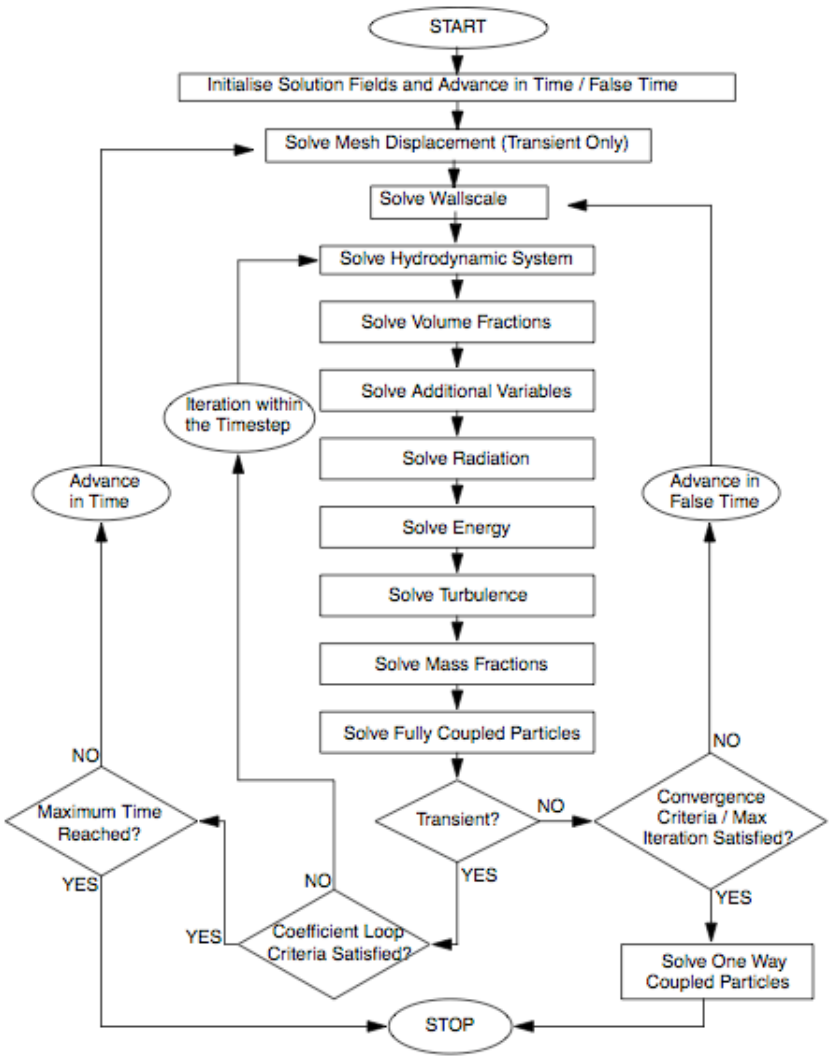

Figure 4.4: Solver flow chart

4.2.2 Linear equation solution

CFX uses a Multigrid (MG) accelerated Incomplete Lower Upper (ILU) factorisation technique for solving the discrete system of linearised equations. It is an iterative solver whereby the exact solution of the equations is approached during the course of several iterations.

The linearised system of discrete equations described above can be written in the general matrix form

$$[A]\,[\phi] = [b]$$

where $[A]$ is the coefficient matrix, $[\phi]$ the solution vector and $[b]$ the right hand side.

The above equation can be solved iteratively by starting with an approximate solution, f^n, that is to be improved by a correction, ϕ' , to yield a better solution, f^{n+1}, i.e

$$\phi^{n+1} = \phi^n + \phi'$$

where ϕ' is a solution of

$$A\dot{\phi}' = r^n$$

with r^n, the residual, obtained from,

$$r^n = b - A\phi^n$$

Repeated application of this algorithm will yield a solution of the desired accuracy.

4.2.3 Residual and imbalance

As described above, the raw residual, $[r]$, is calculated as the imbalance in the linearised system of discrete equation. The residual of an equation identifies by how much the left-hand-side of the equation differs from the right-hand-side at any point in space. If the solution is exact, then the residual is zero. Exact means that each of the relevant finite volume equations is satisfied precisely. However, because these equations only model the physics approximately, this does not mean that the solution exactly matches what happens in reality. If a solution is converging, residuals should decrease with successive timesteps. The raw residuals are then normalised for the purpose of solution monitoring and to obtain a convergence criteria.

For each solution variable, ϕ, the normalised residual is given in general by:

$$[\widetilde{r}_\phi] = \frac{[r_\phi]}{a_p \Delta\phi}$$

where r_ϕ is the raw residual control volume imbalance, a_p is representative of the control volume coefficient and $\Delta\phi$ is a representative range of the variable in the domain.

The RMS residual is obtained by taking all of the residuals throughout the domain, squaring them, taking the mean, and then taking the square root of the mean. This should present an idea of a typical magnitude of the residuals.

While the imbalances are the normalized sum of the flows for a given equation on a particular domain. The absolute flow is normalized by the maximum flow, calculated by looking at flows on all domains for that particular equation.

Chapter 5

Mesh generation

Mesh generation is the process that produces discretization of the computational domain. A complex domain is divided into volumes, called elements or cells, with simpler shape and a local topology. The elements have some basic characteristics, they must be connected to each others but do not intersect and they have to cover the whole domain. Generating a calculation grid for industrial applications is usually the most time consuming part of the CFD analysis and it is crucial in order to achieve correct results.

5.1 Structured and Unstructured grids

Various forms of cells can be used. However, the most common type in CFD programs is a hexahedron with eight nodes, one at each corner, or a tetrahedron with four nodes and four triangular faces (figure 5.1). Two distinct categories of grids exist: structured or unstructured meshes. A structured mesh is composed by an identical pattern of elements connected to any internal node. In 3-D the hexahedral cell is used to compose structured meshes and 8 cells are connected to each internal node of the domain.

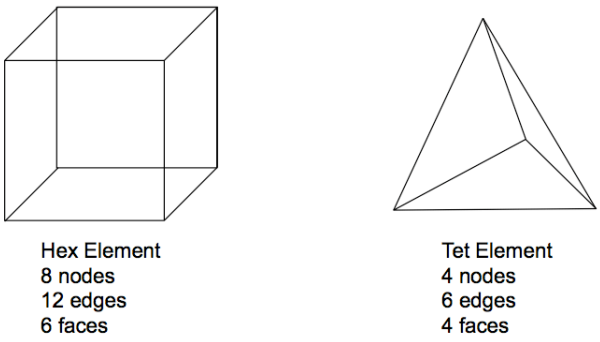

Figure 5.1: Hexahedral and Tetrahedral elements

This method is very suitable for CFD calculations but there is no automatic procedure capable of generating a good-quality grid for complex geometry. Hence it takes a large amount of man-hours to create this sort of mesh. A less time-expensive choice could be the unstructured methods. The most used type of unstructured grid consists of tetrahedral elements. The great advantage of unstructured grids is that they can be easily generated for nearly any desired geometry. The grid generation process is almost completely automatic but still it may require considerable user interaction to produce grids with acceptable degrees of local resolution while at the same time having a good quality of the mesh. They have more local control: elements can be rapidly inserted or removed and connectivity upgraded. In this way certain requirements of node distribution and element sizing is meet easier and the modification stay local without propagating in the whole domain. The main problem in utilizing unstructured meshes is the less accuracy they have especially in the CFD field.

5.2 Hexahedral structured mesh

A critical role is played by grid resolution and grid quality in order to obtain accuracy especially in viscous flow calculations inside the boundary layer close to solid surfaces. The mesh size and shape should be such that it can capture the proper physical conditions that occur in the flow. In general a large amount of points is required in regions of the domains where large gradients exist. The real problem is that we do not always know where the large gradients are. Usually, along the solid surfaces, where the boundary layer is developed, we need to put more points close to the wall in the direction normal to the surface. Grid refinement is needed to resolve important flow details and it is generally

needed not only near walls but also near stagnation points, in separation regions, and in wake regions. By increasing number of nodes better accuracy is achieved. Solution should always (if possible) be based on grid independence tests with same style and mesh arrangement.

For all these reasons hexahedral elements are naturally suitable for numerical analysis of CFD with finite-volume method at least close to solid surfaces (hybrid meshes). In numerical solution of Navier-Stokes equations, the flow is usually parallel to solid boundaries and and viscous effects are pronounced inside the boundary layers. Parallel and high quality meshes are required in such regions. These requirements include smoothness of cell sizes, control of position of the first mesh point close to wall (depending on type of turbulence model), limitation of stretching ratio that must range within certain values, ect. This details can be captured better by hexahedral elements. In fact utilizing tetrahedral grid element it is more complicated to meet these requirements, in particular it is difficult to represent an accurate propagation of the flow along one direction, because these cells have no parallel faces, and they naturally increase numerical approximation errors. Another strong advantage of hexahedrons is that for a certain number of nodes, fewer elements are required to mesh a domain. It means that less memory is used for the mesh and solution data storage and a shorter time is required to compute the solution. Unfortunately, structured grids tend to contain too many cells in regions where it is not necessary. In order to generate more cells in a certain region, new grid lines should be introduced along the entire computational domain in corresponding direction, which usually results in overpopulation of cells in regions where it is not desired. Block-structured methods can resolve this drawback to some degree but they still provide limited flexibility within one block.

5.2.1 Block-structured mesh

When the geometry is complex, it is very difficult to generate a single zone grid with adequate control on the distribution of the mesh points using structured grids. In this context we utilize block structured meshes which allow for a good quality control and a local mesh refinement without exceeding too much in number of cells. The CAD geometry which composes the computational domain is divided in hexahedral blocks which represent the block topology model. Each block vertex, edge, surface or volume can be associated to a relevant geometric entity in order to perfectly describe complex features in the domain. Once the block topology model is created it may be further sub-devided through the splitting edges and faces. On each block the number and distribution of internal cells is controlled by

imposing the number of node on the edges and specifying bunching requirements which follow particular meshing distribution laws. Practically refinement or coarsening of the mesh is specified for any block region to allow a finer or coarser mesh definition in areas of high or low gradients, respectively. The geometry we have to mesh is complicated hence in order to accurately refine the grid around the nacelle, especially in the boundary layer zone and at the leading edge, without propagating the refinements throughout the whole domain, a particular type of blocking technic is adopted: the O-grid. This technique is employed when you desire a circular mesh either around a localized geometric feature or globally around an object. The O-grid is simply the modification of a single block or blocks to a 5 sub-block topology as shown in figure 5.2. There are several variations of the basic O-grid generation technic as shown in figure. For example it can be created entirely inside the selected block or such that the O-grid passes through the selected block faces as we can see below. We have used mapped blocks, hence if you set edge parameters on a mapped face edge, opposite edges will have a similar number of nodes and if you split a block that action will propagate through faces that have a mapped relationship on the opposite side.

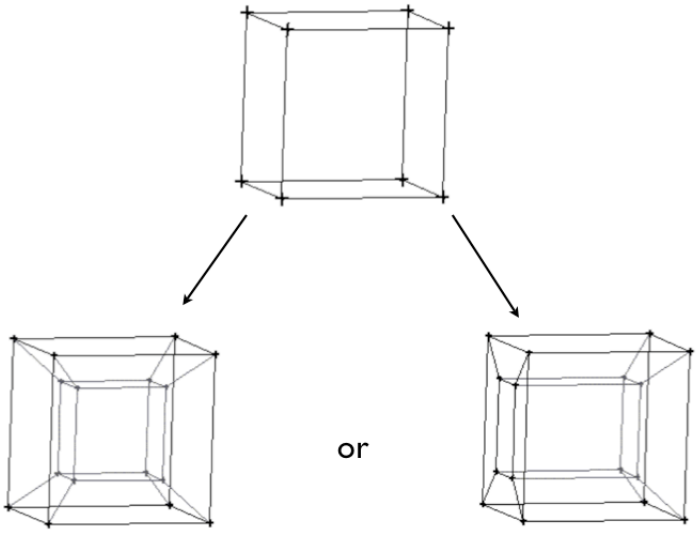

Figure 5.2: O-grid blocks

5.2.2 Mesh quality criteria

During mesh generation, elements which are of poor quality or even invalid (concave or inverted) are often produced. In general, such elements degenerate accuracy of computations. Hence, invalid elements should not be allowed to exist in final meshes, while quality

of valid elements should be improved as much as possible. The mesh quality criteria we have imposed are:

Angle $>$ 15° Checks the minimum internal angle for each element, with 0 as degenerate and 90 as perfect.

Aspect Ratio $>$ 0.3 For hexahedral elements, the aspect ratio is defined as the size of the minimum element edge divided by the size of the maximum element edge. The values are scaled, so that an aspect ratio of 1 is perfectly regular, and an aspect ratio of 0 indicates that the element has zero volume.

Determinant (2x2x2 stencil) $>$ 0.3 The Determinant, more properly defined as the relative determinant, is the ratio of the smallest determinant of the Jacobian matrix divided by the largest determinant of the Jacobian matrix. In this option, the determinant at each corner of the hexahedron is found. A determinant value of 1 would indicate a perfectly regular mesh element, 0 would indicate an element degenerate in one or more edges, and negative values would indicate inverted elements.

5.3 Generation of the calculation grid

In order to completly understand the procedure we have to introduce the geometric and block topology entities.

The geometric data are:

- Points: x, y, z point definition
- Curves : trimmed or untrimmed NURBS curves
- Surfaces: NURBS surfaces, trimmed NURBS surfaces

The block topologic data are:

- Vertices: corner points of blocks, of which there are at least eight, that define a block
- Edges: a face has four edges and a block twelve
- Faces: six faces make up a block
- Blocks: volume made up of vertices, edges and faces

The meshing procedure can be summarized in the following steps:

1. In CATIA v5 we create our CAD model of half of a nacelle. We import the geometry file of the nacelle in ICEM (figure 5.3).

2. We clean the possible topology errors generated during the importation and with the geometrical tools of ICEM we create the external boundaries of the domain and the symmetry plane (figure 5.3).

3. We creates one block that encompasses the entire geometry and we associate the block faces to the external boundary surfaces of the domain (figure 5.4).

4. We split the main block in 18 blocks, in this way we have a central block which represents the nacelle (figure5.4).

5. We utilize the O-grid generation technique on the block representing the nacelle in order to create the boundary layers blocks all around the nacelle surface (figure5.5). As we can see in figure we have generated a sheet of thin blocks which surrounds the internal and external surfaces of the nacelle. Depending on what kind of operations we use to generate new blocks the rest of the blocking model all around the nacelle is automatically modified in order to preserve a correct topologic structure (figure 5.6).

6. Interactively we define new blocks through split, merge, O-grid definition, edge/face modifications and vertex movements and we associate the blocks entities to the important geometric features.

7. We check the blocks quality to ensure that the block model meets specified quality thresholds.

8. We assign edge meshing parameters such as maximum element size, initial element height at the boundaries and expansion ratios (figure 5.6 and 5.7).

9. We generate the mesh (figure 5.8). Interactively we check the mesh quality and make modifications on the blocking, on the association of blocking to geometry and on the distribution of mesh nodes on the edge to ensure that specified mesh quality criteria are met. The most critical zone to be meshed is the boundary layer where the viscous phonomena take places and the gradients normal to the surface are important. Especially around the trailing edge of the nacelle where model has a pronounced curvature, we have to concentrated a large number of cells.

10. Write Output files to the desired solvers.

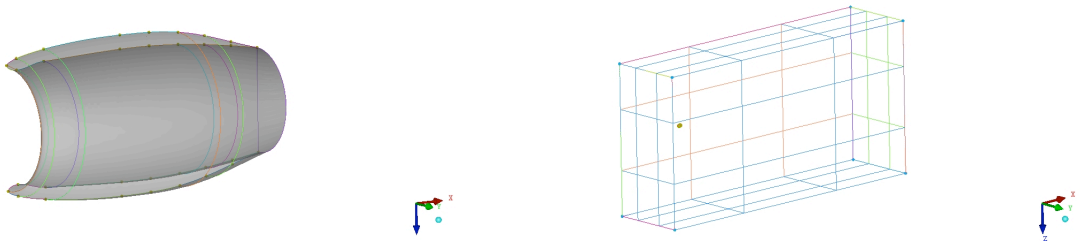

Figure 5.3: Meshing procedure: step 1 and 2

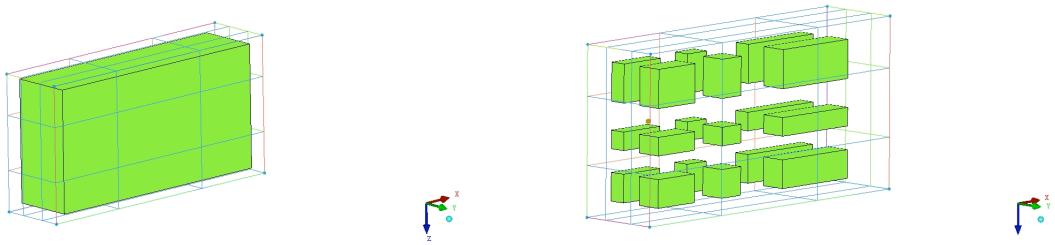

Figure 5.4: Meshing procedure: step 3 and 4

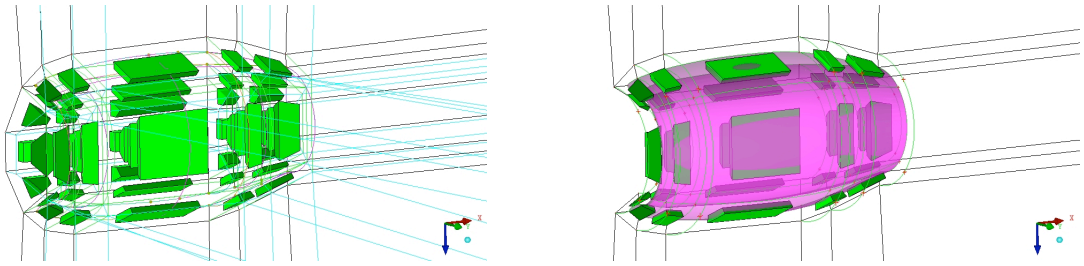

Figure 5.5: Meshing procedure: step 5

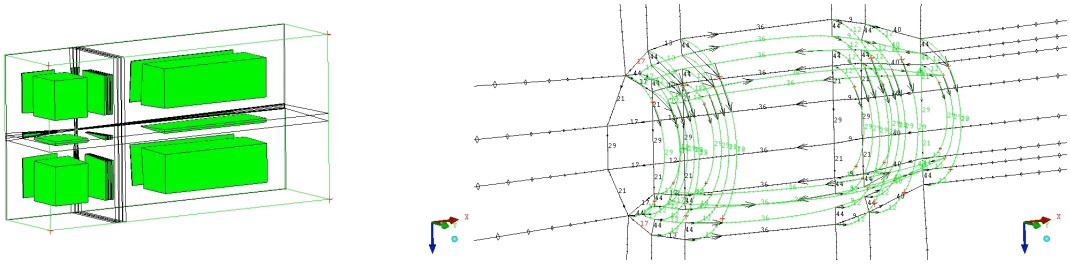

Figure 5.6: Meshing procedure: step 5 e 8

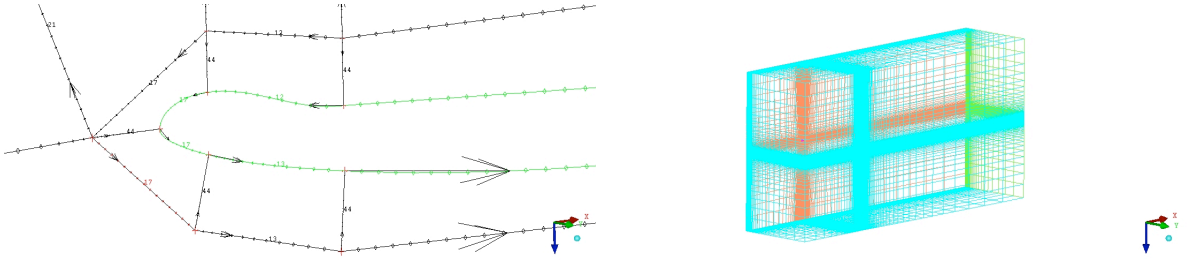

Figure 5.7: Meshing procedure: step 8 e 9

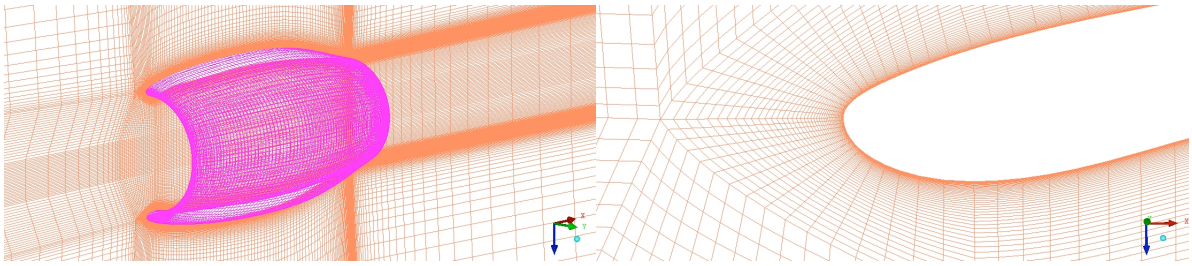

Figure 5.8: Meshing procedure: final mesh and lip zone enlargement

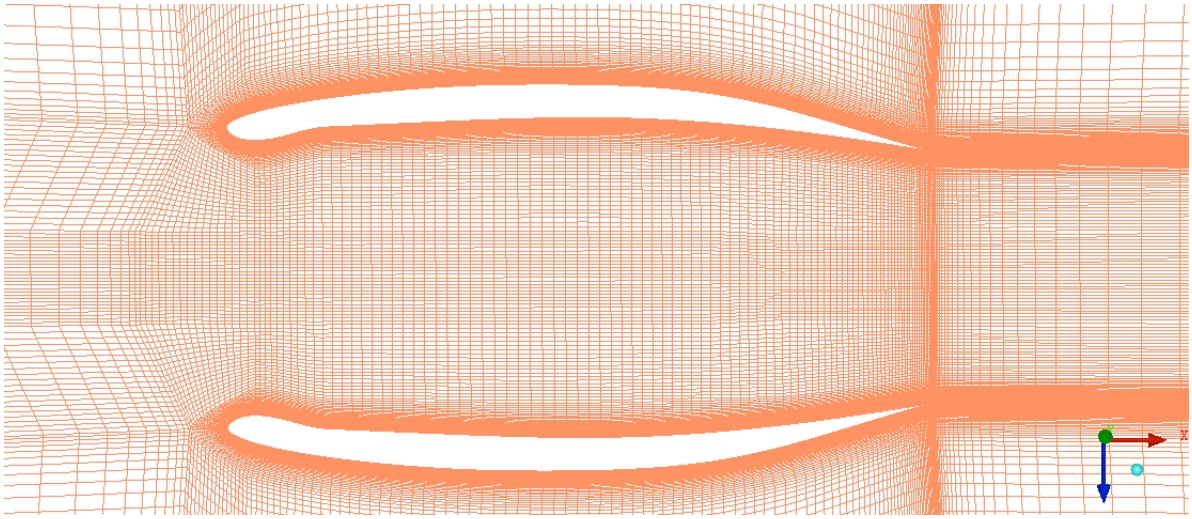

Figure 5.9: Meshing procedure: final mesh, symmetry plane

5.3.1 Mesh models

The procedure previously described has been applied to a specific nacelle model called "empty nacelle", this is the simplest model where the flow could pass thought the engine. As we are going to explain in the next section we utilize the results of our CFD simulations in order to investigate the impact of the nacelle design on the flow, hence after every geometric change logically we perform specific modification on the blocking model and on the mesh. All the meshes derive from a 2 millions volumes basic mesh. When we create models more and more complicated, adding different new structures to the basic nacelle, the cells number could vary. As results of the geometric modifications sometimes we have heavily changed the distribution and shape of the blocks. Figures 5.10 show the blocking models and the respective meshes (the 2-D mesh projection on the symmetry plane) for other nacelle configurations that we studied.

5.3.2 Definition of y^+

y^+ is a dimensionless quantity which used to evaluate the suitability of a CFD mesh used to obtain a certain solution. It is defined as:

$$y^+ = \frac{\sqrt{\tau_\omega/\rho} \bullet \Delta n}{\nu} \tag{5.1}$$

where Δn is the distance between the first and second grid points off the wall and $\tau_\omega$is the wall shear stress. It can only be calculated a posteriori and it is not easy to predict his value on the entire desired surface when the geometry is complicated. We will consider acceptable a mesh whose solution has a y^+ value inferior to 50 over the whole nacelle model.

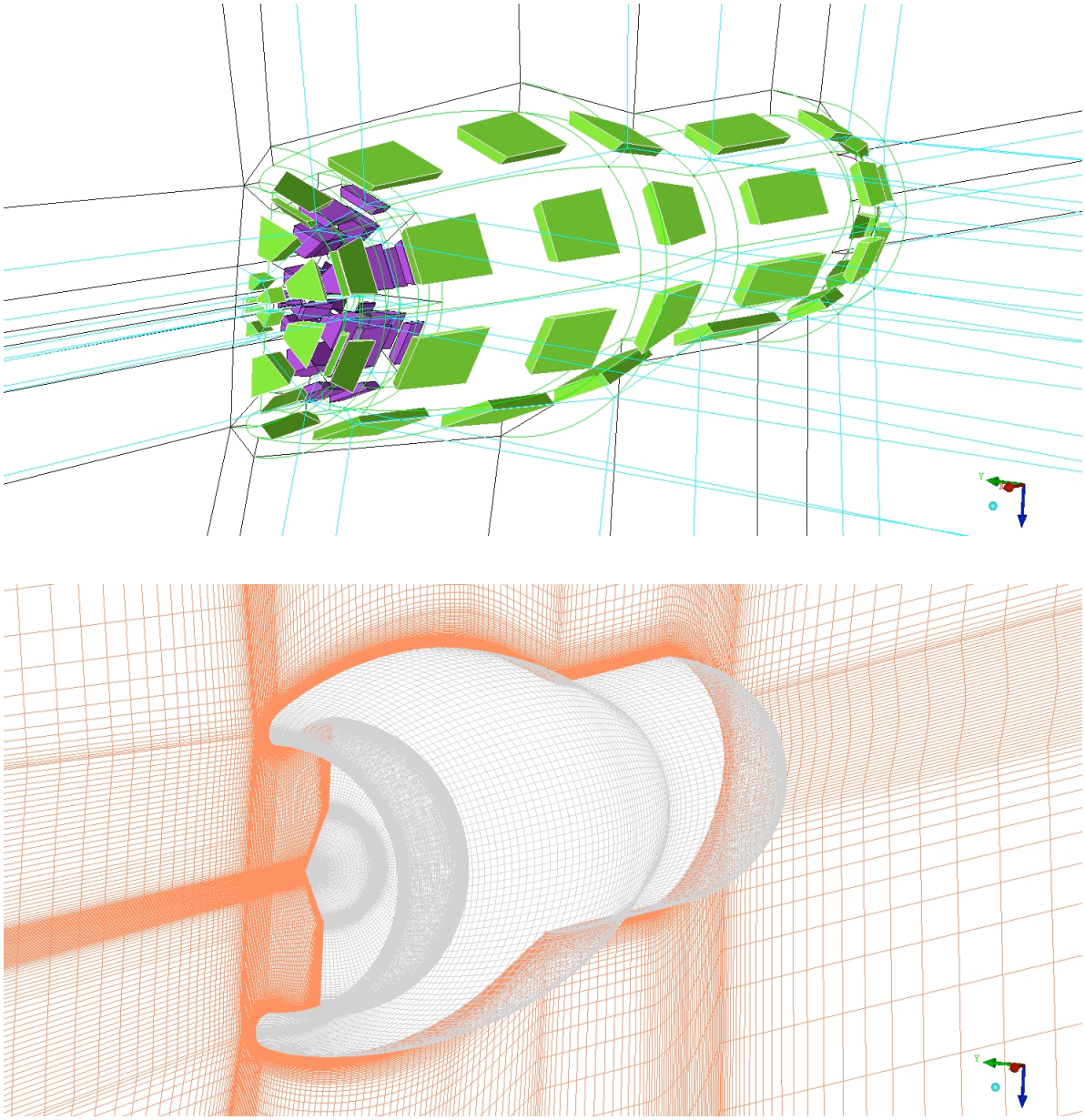

Figure 5.10: Different model blocking and mesh

Chapter 6

Numerical results

Once the meshing process has been completed, the next task consists in the realisation of a series of numerical simulations that lead to the determination of the flow field. In this section we are going to describe our methodology of work. As we already explain in section 1 our scope is to understand the phenomena of the flow which take place at the inlet of the nacelle, just before the hypothetical surface representing the rotor. We will test different geometric configurations and boundary conditions trying to find in which way they influence the separation.

6.1 General pre-processing configuration

The mesh file generated with ICEM is imported in CFX-Pre as we already show in section 2. Figure 6.1 shows the computational domain. The fluid domain is composed by air describe as an ideal gas with property summarized in table 6.1. The domain is delimited by 5 external surfaces named INLET, OUTLET, BOTTON, TOP, SYMMETRY and SIDE. The nacelle surface is named WALL and depending on the model configuration we have the presence of another surface placed inside the nacelle, perpendicular to engine axis which represents the the fan. It is named FAN. All simulations are Steady state. Steady conditions are reached after a relatively long time interval when the solution is converged. The variables do not change with time and they therefore require no real time information to describe them. The adopted turbulent model was the $k-\omega$ SST with automatic wall function and an initial turbulence intensity of 5%. On each boundary surface we impose different boundary conditions depending on which kind of simulation we carried out. We list now all sorts of conditions we have used.

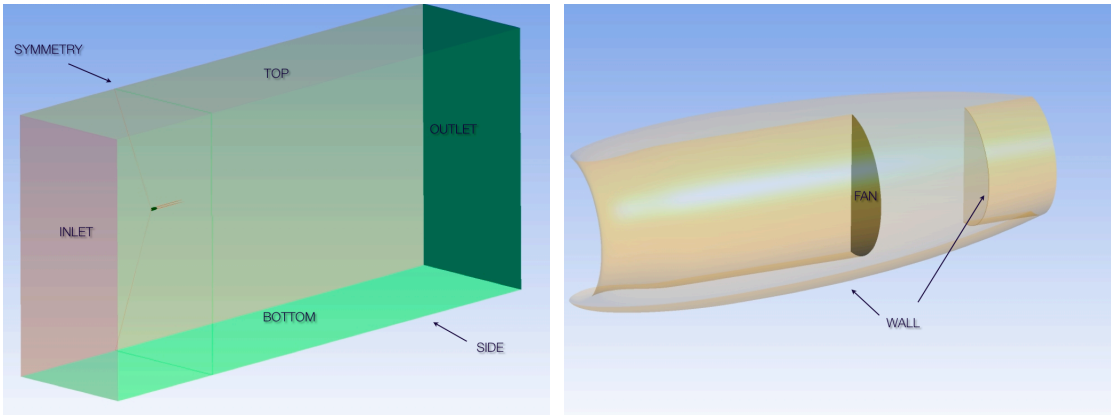

Figure 6.1: Computational domain

Specific heatCp	Molar mass	Reference T	Reference P	Reference ρ
$1004 \frac{J}{KgK}$	$28.96 \frac{Kg}{Kmol}$	$25°C$	$1\ atm$	$1.185 \frac{Kg}{m^3}$

Table 6.1: Property of air

6.1.1 Boundary conditions

Boundary conditions are a set of properties or conditions on surfaces of domains, and are required to fully define the flow simulation. The type of boundary condition that can be set depends upon the bounding surface.

Fluid boundary

An external surface of a fluid domain is called fluid boundary and it supports following boundary conditions:

• Inlet - An inlet boundary condition is used where the flow is predominantly directed into the domain.

• Outlet - An outlet boundary condition is used where the flow is predominantly directed out of the domain.The hydrodynamic boundary condition specification (that is, those for mass and momentum) for a subsonic outlet involves some constraints on the boundary static pressure, velocity or mass flow. For all other transport equations, the outlet value of the variable is part of the solution.

• Opening - An opening can be used at a boundary where the flow is into and/or out of the domain. The opening boundary condition type is only available for subsonic boundaries.

- Wall - Impenetrable boundary to fluid flow.
- Symmetry Plane - A plane of both geometric and flow symmetry.

Solid boundary

A solid boundary is an external surface of the solid domain and supports the following boundary conditions:

- Wall - Impenetrable boundary to fluid flow.
- Symmetry Plane - A plane of both geometric and flow symmetry.

6.1.1.1 Subsonic inlet

Cartesian Velocity Components

We specify the boundary velocity components on the entrance of the domain.

$$\mathbf{U}_{inlet} = U_{spec}\mathbf{i} + V_{spec}\mathbf{j} + W_{spec}\mathbf{k} \tag{6.1}$$

Total Pressure

We impose the total pressure P_{tot} at an inlet boundary condition, and the static pressure needed to properly close the boundary condition is computed by the solver.

We can also specify the direction vector of the flow in terms of its three components. For this kind of condition the mass flow on the boundary is an implicit result of the flow simulation.

Static Temperature

If we specify the static temperature T_{stat} at the inlet energy flow Q_{inlet} entering the domain is composed by

$$Q_{inlet} = Q_{advect} + Q_{diffus} \tag{6.2}$$

We can assume the diffusion term Q_{diffus} to be negligible compared to the advection term Q_{advect}. This last term is a function of the total enthalpy h_{tot}

$$Q_{advect} = \dot{m}h_{tot} \tag{6.3}$$

where

$$h_{tot} = h_{stat} + \frac{1}{2}U^2 \tag{6.4}$$

where U is the boundary inlet velocity calculated with the mass and momentum boundary condition and h_{stat} is computed using the imposed static temperature T_{stat} the boundary values of $U$and p and the constituitive equation 3.9.

Total Temperature

We can alternatively impose the total temperature T_{tot} and calculate the static using

$$T_{stat} = T_{tot} - \frac{U^2}{2C_p} \tag{6.5}$$

In order to calculate he boundary advection and diffusion terms the procedure is similar to the one used for specified static temperature.

6.1.1.2 Outlet

Uniform Static Pressure

Using this boundary condition we are specifying the static pressure p_{stat} over the outlet boundary surface.

Average Static Pressure

We impose the average value $\overline{p}_{stat}$ considering the integral over the entire outlet surface:

$$\overline{p}_{stat} = \frac{1}{A}\int_S p_n dA \tag{6.6}$$

where p_n is the effective pressure profile and it can float while the imposed average static pressure stays constant.

Mass Flow Rate : Scale Mass Flows

The total mass flow rate $\dot{m_{tot}}$ through the outlet boundary can be imposed. In this way the outlet boundary velocity is part of the solution.

At each integration point the solver calculates the local mass flow rate distribution:

$$\dot{m_{ip}} = \rho_{ip} A_{ip} U_{ip} \tag{6.7}$$

From that distribution we calculate the estimated total mass flow rate through the outlet boundary condition:

$$\dot{m}_{tot}^{est} = \sum_{all} \dot{m}_{ip} \tag{6.8}$$

where the summation is over all boundary integration points. At each iteration a scaling factor F is calculated and used to scale the local integration point mass flows:

$$F = \frac{\dot{m}_{tot}}{\dot{m}_{tot}^{est}} \tag{6.9}$$

where F can be greater than or less than unity during the computation. The final integration point mass flows are reset by multiplying the integration point mass flows by the scaling factor:

$$\dot{m}_{ip} = F \rho_{ip} A_{ip} U_{ip} \tag{6.10}$$

In this way the mass flux profile is an implicit result of the solution and at the same time gives exactly the specified mass flow rate. However, the lack of robustness of this condition, especially in the initial phase of a simulation, makes it difficult to use.

6.1.1.3 Wall

No Slip

The wall is not moving and the velocity of the fluid at boundary the is set to zero:

$$U_{wall} = 0 \tag{6.11}$$

Adiabatic

The adiabatic wall boundary condition allows no heat transfer across the wall boundary:

$$Q_{wall} = 0 \tag{6.12}$$

6.1.1.4 Symmetry plane

A problem is symmetric about a plane when the flow on one side of the plane is a mirror image of flow on the opposite side. By definition, a symmetry boundary condition refers

to a planar boundary surface. and the normal velocity component U_n at the symmetry plane boundary is set to zero:

$$U_n = 0 \tag{6.13}$$

and all the other scalar variable (p, T, ρ, h) gradients normal to the surface are set to zero:

$$\frac{\partial \psi}{\partial n} = 0 \tag{6.14}$$

6.1.2 Visualization of separated flows

In order to understand the separation phenomena and its influence on the engine fan we have to be capable of define and visualize it. There is no precise mathematical definition of separations in 3-D flows, but commonly there are qualitative descriptions of separations concerning flow turning away from a surface where it had been moving tangentially. While in 2-D we can easily define the separation points as the critical point on a one dimensional boundary where flows in opposing directions converge and consequently the wall shear stress is zero. The wall shear stress is defined as the normal derivative to the surface of the velocity vector field. In 3-D the zone where flows with opposing directions meet is identify by a line on the 2-D boundary and the wall shear stress criterion can not be applied because there is almost always flow along the separation line and the it will never be exactly zero. Anyway we will use a phenomenological qualitative approach in order to identify the separations zone, observing the flow patterns trying to identify the skin friction lines and analyzing the wall shear stress distribution on the inlet surface. The skin friction lines are streamlines constrained to the body, the separation lines is a particular friction line going through a saddle point.

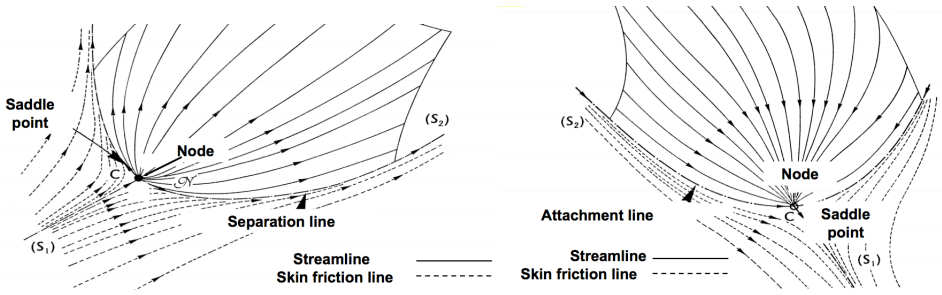

Figure 6.2: 3-D separation characteristic (figure from Onera archive)

6.2 Incompressible flow simulation

Initially we run simulations considering an incompressible flow. We were aware of the possibility of compressible phenomena appearance, especially in the inlet zone where the flow accelerates, but we assume a simplified and numerically faster model in order to investigate certain design aspects where the difference between compressible and incompressible flow was not fundamental. For all incompressible simulations we impose a constant air temperature equal to the Reference T , and a constant air density equal to the Reference ρ. The boundary surfaces INLET, SIDE, BOTTOM and TOP are all specify as inlet boundary type with imposed cartesian velocity components corresponding to a far field velocity of 77m/s with an angle with respect to x axis of 25°. The OUTLET surface is assigned as outlet boundary condition with an average static pressure on the whole surface of 0 Pa.

Given the symmetry of the problem we impose a symmetry-plane type condition on SYMMETRY and carried out simulations on half domain. We always consider no slip wall and adiabatic wall condition on WALL without taking in account the effect of roughness.

We run four kind of incompressible simulations and for each case we impose different conditions on the surface FAN, when it was present:

- a case with an empty nacelle without FAN.
- a case with a FAN surface inside the nacelle simulating the presence of the engine's rotor.
- an analysis of the influence of the mass flow value on the separation strength for a nacelle configuration with a covering nose.
- an analysis of the model for the exit nozzle of the nacelle.

6.2.1 Empty nacelle

We consider an empty nacelle hence the FAN surface is not present. This simulation was run in order to test the suitability of the far field boundary condition, to understand the basic features of the flow separation and the way to quantify it, to understand the association of the separation with the distortion phenomenon, and evaluate an initial position for the FAN surface. In order to judge the convergence (or divergence) and the progress of a solution, residual monitor plots, together with the monitoring of quantities of engineering interest, are produced and updated every time an iteration is completed. These equations are determined by the model selection previously made. Figure 6.3 shows the convergence for mass and momentum equation, plotting root mean square residuals of p (mass equation) and velocity components U, V, W (momentum equation). We can also see the imbalance for the same variable p, U, V, W. According to the monitors less than fifty

iterations are sufficient to reach the convergence, providing a steady solution.

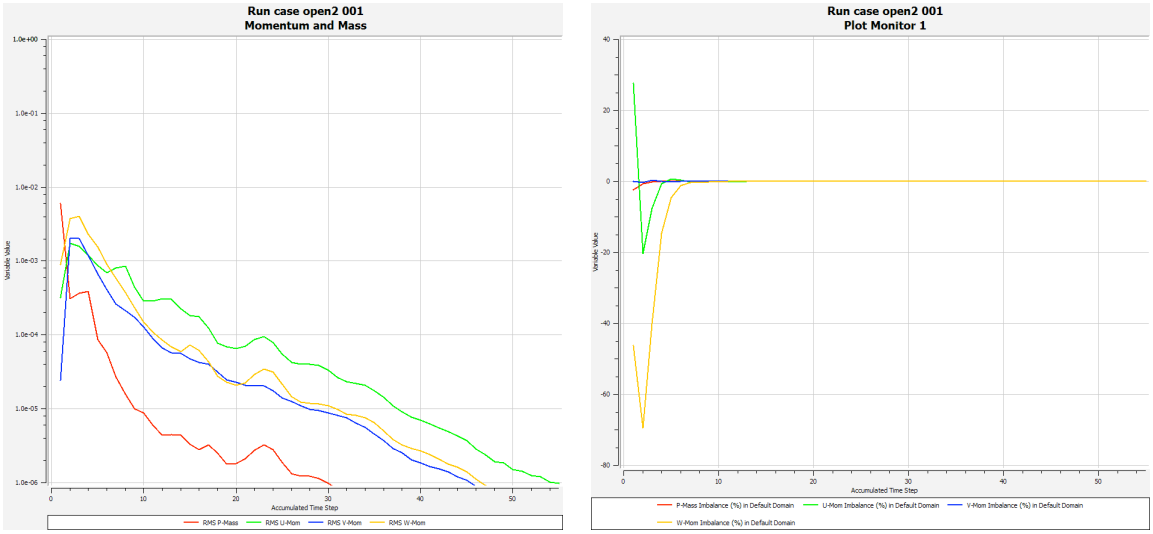

Figure 6.3: Monitor residuals and imbalance for empty nacelle

Figure 6.4A represents the contours of velocity magnitude on the symmetry plane with the superposition of streamlines, while figure 6.4B shows just the negative velocity x-component. The flow approaching the nacelle inlet with an angle of attack of 25° decelerated. Leaving the stagnation point it then accelerates around the lip both inside and outside the nacelle. After the solid body the flow returns to be straight and leaves the domain with same 25° angle with respect to x-direction. We clearly see the presence of a massive separation bubble which almost cover the entire nacelle, with a reverse flow region where x-components of velocity are negative.

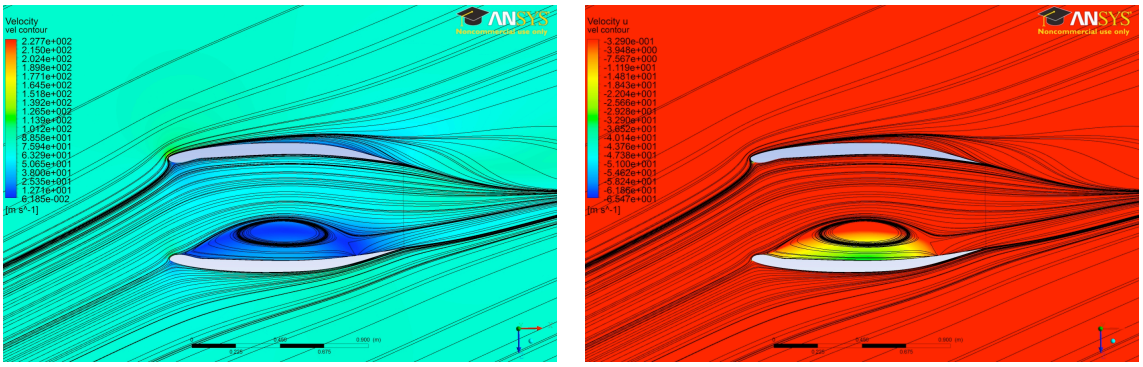

Figure 6.4: Streamlines and velocity magnitude (left A) and x-component (right B) contours for emptry nacelle

Figure 6.5 shows the internal friction lines. As we already anticipate they can be used to evaluate the dimension of the separation zone on the surface inside the nacelle. We notice also the presence of a smaller separation on the external surface of the nacelle. We calculate the mass flow passing through the surface on the exit plane. It is $\dot{m} = 5.67$ m/s.

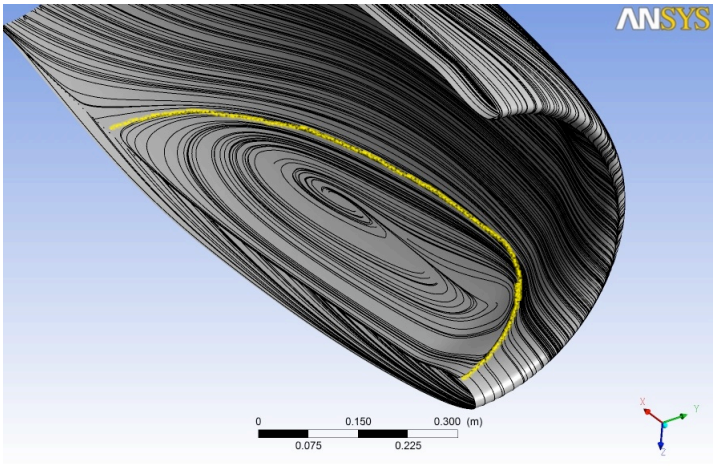

Figure 6.5: Skin-friction lines and highlighted lines of detachment and reattachment

We finally plot the total pressure distribution on a virtual plane which represent the place where we are going to impose the FAN boundary surface in order to simulate the presence of the engine (figure 6.6). The presence of the flow separation influence the total pressure filed introducing a distortion.

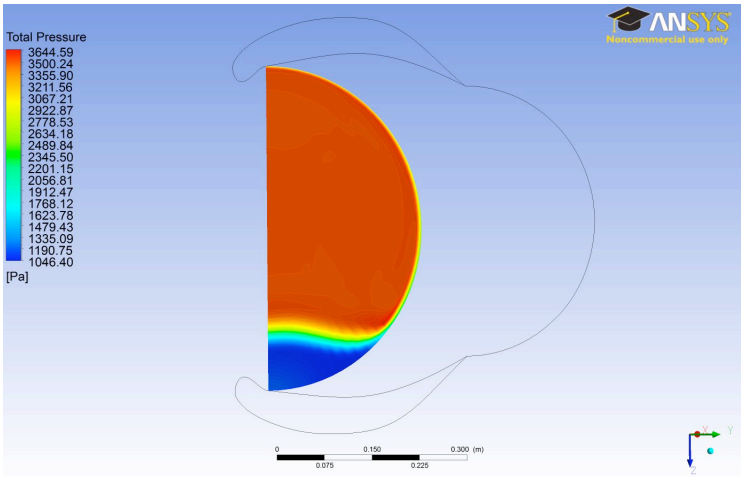

Figure 6.6: Total pressure contour on rotor virtual plane

6.2.2 Nacelle with internal surface massflow boundary condition

We make the first design modification adding the FAN surface inside the nacelle. It simulates the presence of the engine rotor. We place the new boundary surface in the rearmost position from the real rotor position in order to investigate the flow patterns in that zone without influencing them. We close the nacelle with a semicircular wall on the exit plane. On the FAN we impose a outlet type mass flow boundary condition with a value of 15 Kg/s. The basic features are not changed. The flow enters the inlet and separates once it reached the diffuser. If we compare this situation with the empty nacelle configuration we can see in figure 6.7 that the flow detaches in the same zone but reattaches earlier . As the mass flow increases, the separation extent tends to reduce.

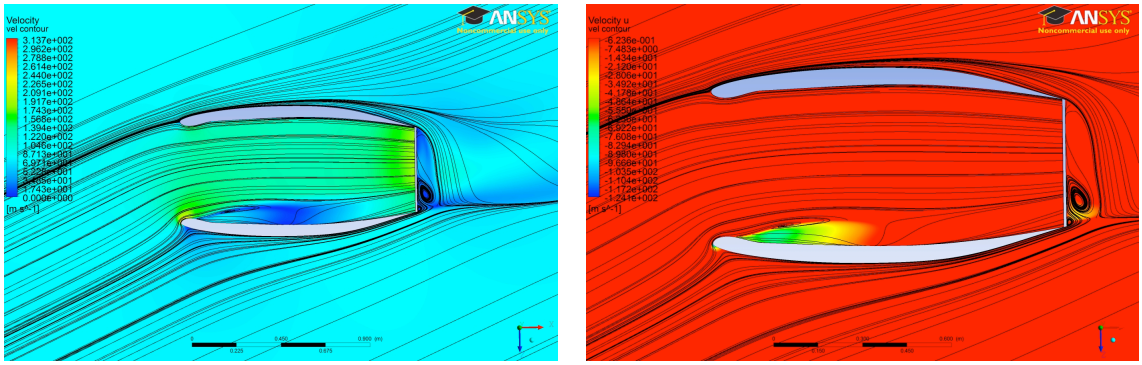

Figure 6.7: Streamlines and velocity magnitude and x-component contours for a nacelle with internal surface massflow boundary condition.

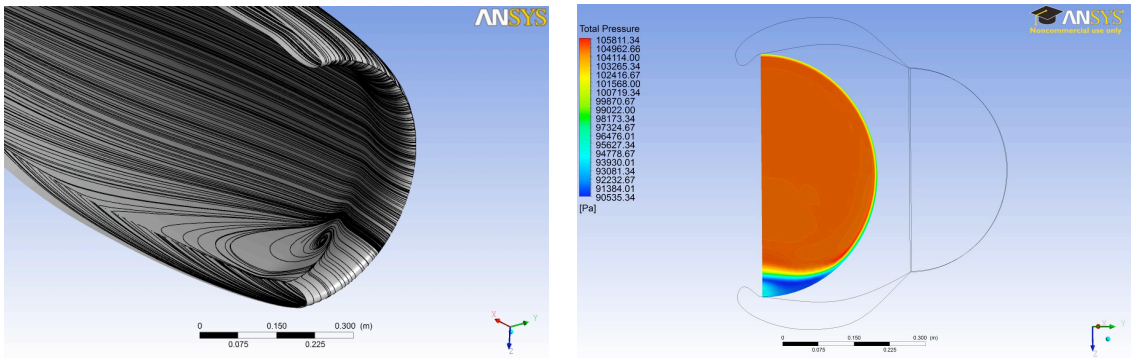

Figure 6.8: Skin-friction lines (left) and Total pressure contour on rotor virtual plane (right) for a nacelle with internal surface massflow boundary condition.

We have a worst and slower convergence due to the numerical problem of using a mass flow boundary condition but mainly because of the presence of a new separation behind

the nacelle exit. The flow can not smoothly turn around the sharp geometry change of the body and separates generating an unstable couple of large eddies.

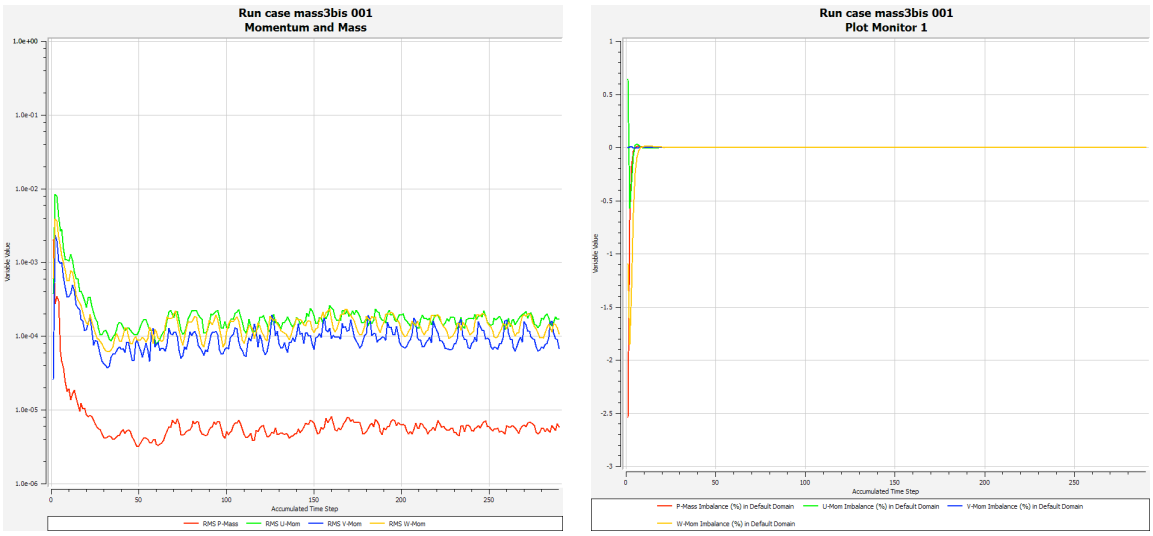

Figure 6.9: Monitor residuals and imbalance for empty nacelle for a nacelle with internal surface massflow boundary condition.

6.2.3 Covering nose and analysis of mass flow variation

Once again we modified the interior geometry affixing a structure representing the cover nose. We designed it as an ellipsoidal cowl mounted on cylinder. The elliptic shape is considered until the virtual plane of the rotor, after that a straight tube attaches the nose to the FAN surface which has become an half of an annulus. We impose now three different values for the mass flow 10 Kg/s, 12.5 Kg/s and 15 Kg/s studying the effect on the detachment dimension and consequently on the distortion. As the mass flow increases, the separation extent tends to reduce (figure 6.10 and 6.11). The total pressure contours show that the higher is the mass flow the smaller is the distorted zone but the greater is total pressure loss.

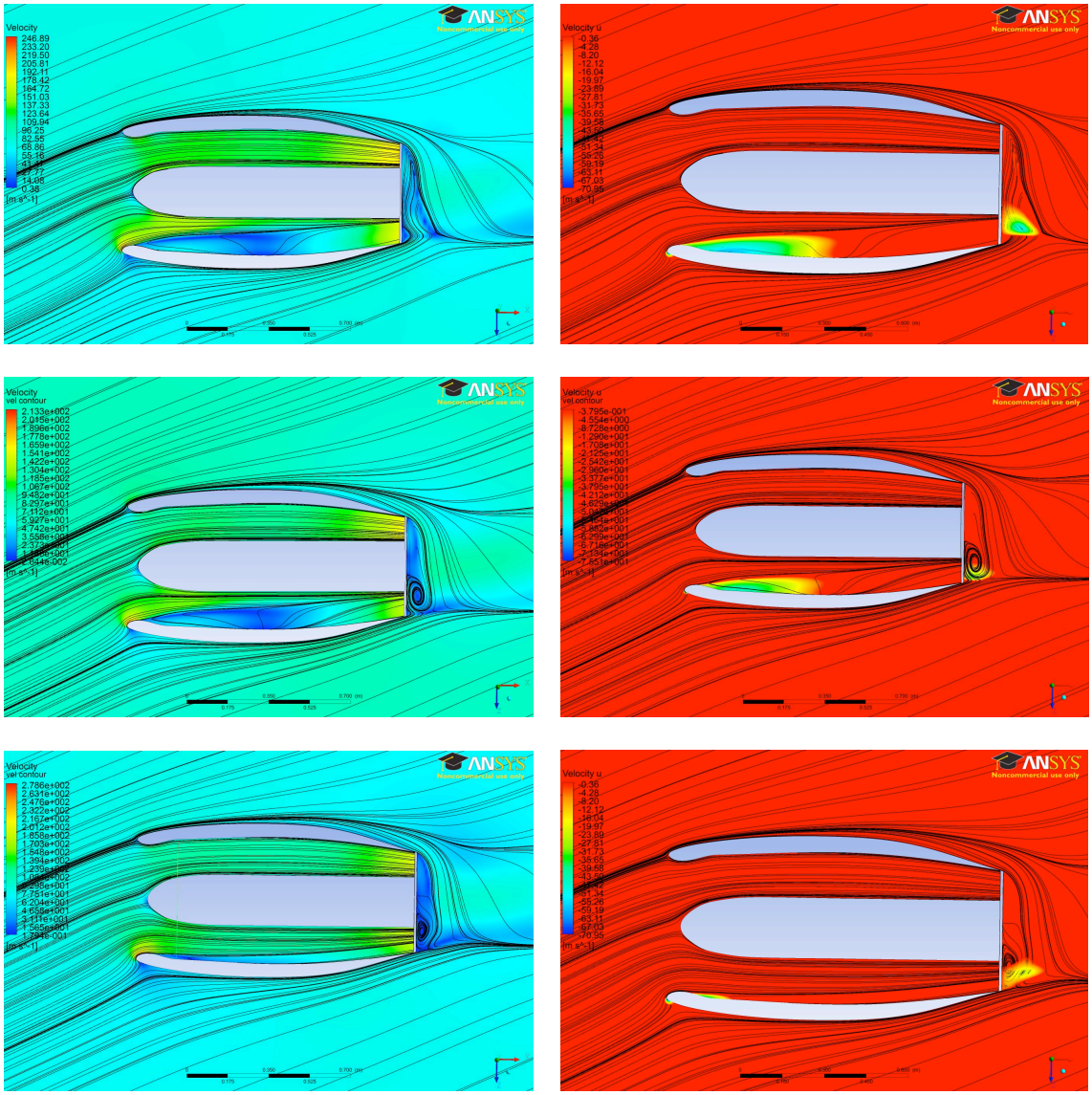

Figure 6.10: Streamlines and velocity magnitude and x-component contours for a nacelle with covering nose an FAN face placed in three different positions.

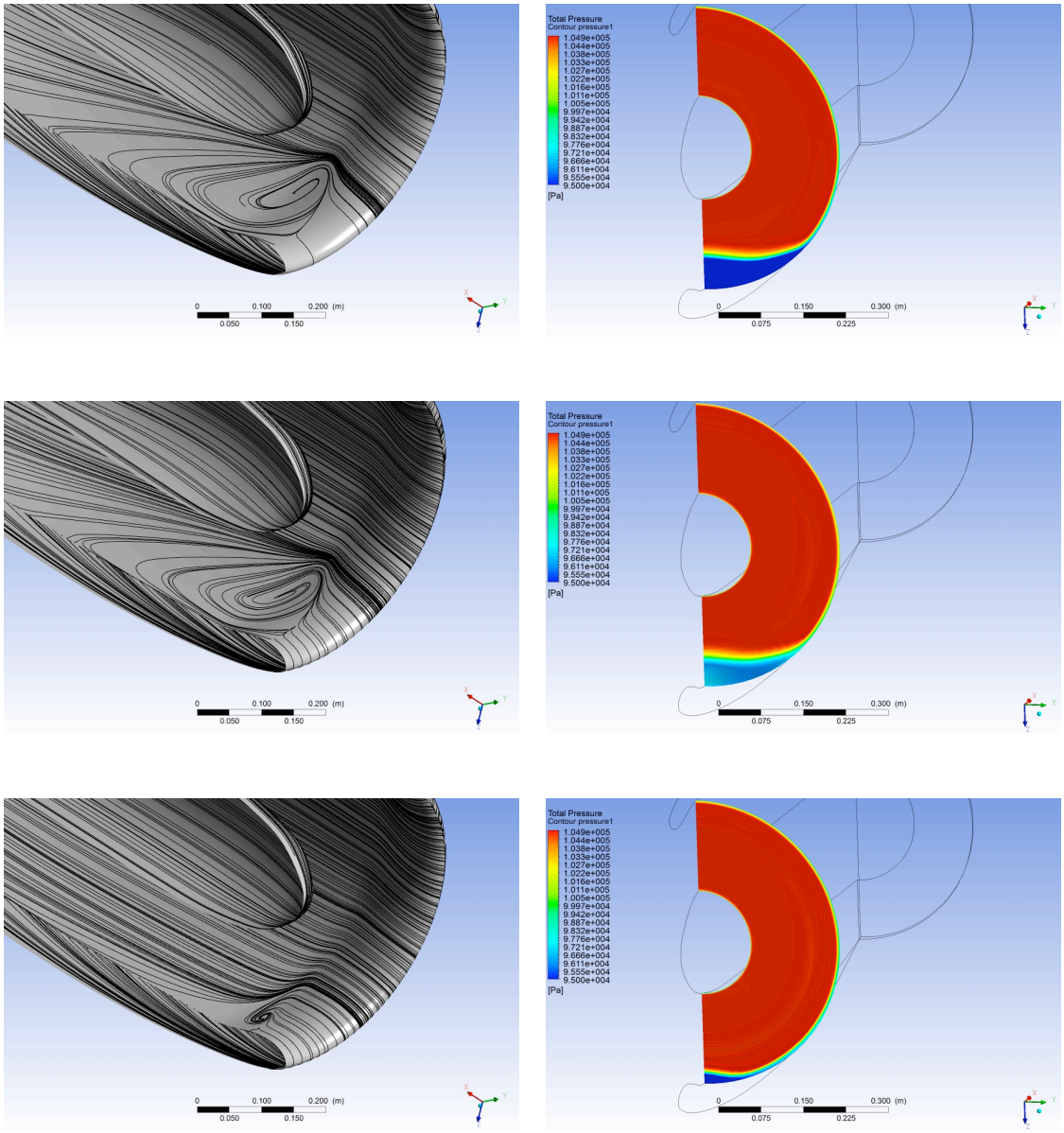

Figure 6.11: Skin-friction line and total pressure contour for a nacelle with covering nose an FAN face placed in three different positions.

6.2.4 Analysis of the nacelle exit

We want to study the configuration of the rear. Our objective is finding a design which would not influence the flow near the region of most interest, the intake, and would give converged and rapid solutions. We test three configurations, presented in figure 6.13 . We also report the residual monitor in figure 6.12. The first configuration is the standard design we have employed in the former simulations. For the others models we imagine of simulating the engine jet modeled shape. A solid generated by the revolution of an ellipse is joined with the exit plane of the nacelle with a cylindrical base solid. We are doing a rough approximation of the flow behind the nacelle but we are not interested in having realistic results regarding this zone, we are just looking for a simple and not time-expensive design capable of increasing the speed of the convergence. We immediately see that the first configuration does not work properly, the flow separates and generate two vortices. The solution is unstable and convergence is deteriorated. We find more rapid and stable solutions for the latter models. Finally we choose the second design because flow approaching the nacelle intake seems to be less deviated from the solid jet and the solution is considered more plausible.

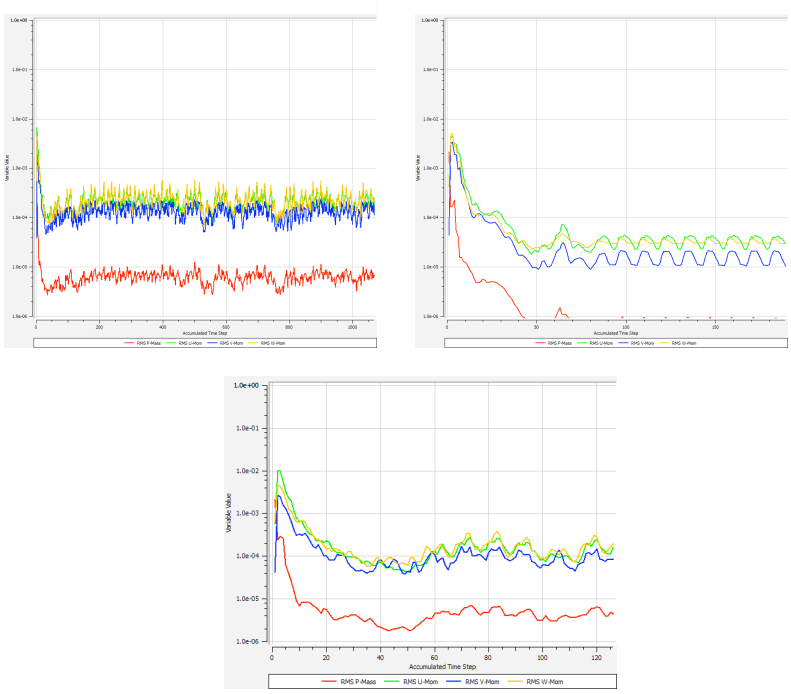

Figure 6.12: Monitor residuals for different rear configurations: no solid jet (left top), small solid jet (right top) and long solid jet (bottom).

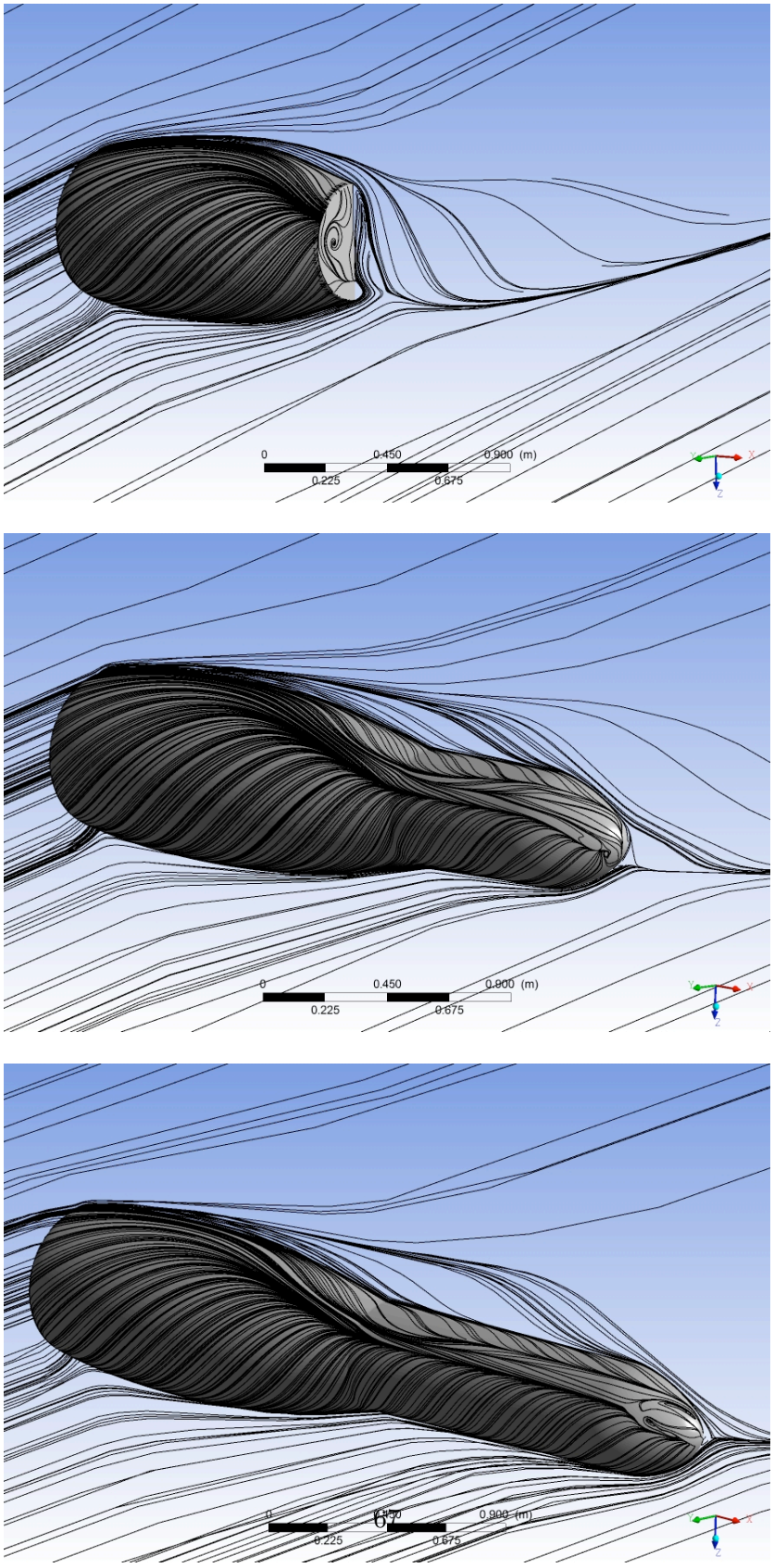

Figure 6.13: Streamlines on symmetry plane and on external surface for different rear configurations

6.3 Compressible flow simulation

Now that we have more informations and we are familiar with the separation mechanism thanks to the previous incompressible solutions we perform more accurate compressible flow simulations. After elaborating the former results we generate a particular design. For the rear part we employ the solid extrusion simulating the jet previously tested. The covering nose is much smaller and conical and the FAN surface is generally placed closer to the virtual rotor plane. For all compressible simulations we consider air as an ideal gas with a reference pressure of 0 atm.

The boundary surfaces INLET and BOTTOM are specify as inlet boundary type with imposed total pressure $Ptot$ = 101325 Pa with fixed flow direction components always corresponding to a far field velocity of 77m/s and angle with respect to x axis of 25°. We also specify the total temperature $Ttot$ = 288 K. The OUTLET and TOP surfaces are assigned as outlet boundary condition with an average static pressure on the whole surface of 97700 Pa. Not only the SYMMETRY but also the SIDE surface is defined as symmetry boundary type.

6.3.1 Test on FAN face boundary condition

In order to impose a constant mass flow, which simulates the presence of the engine rotor, on the FAN face boundary we can follow two approaches. The first one is specifying the average mass flow passing through the surface as in the incompressible cases. The second option is to specify the constant average static pressure p. The difficulty associated with this condition is that it is dependent on the numerical scheme and model used, and the mass flow value is a result of the simulation which yield difficulties in imposing its desired value.

Figure 6.15 represents the contours of Mach number, the skin-friction lines and the distortion for the two boundary cases. The solutions are similar even if the constant pressure case seems to present a smaller separation zone with consequently a less distorted flow. Probably the real cause of these little differences is the oscillating nature of the solutions. Figures 6.14 show in fact that both solutions have very slow convergence. In particular if we control the variables imbalance for the average mass flow case we can see its limited robustness, especially in the initial phase of a simulation. Also the constant pressure case residuals and imbalances oscillate but the solution seems to slowly converge to stable values. This formulation is more robust than the mass flow one.

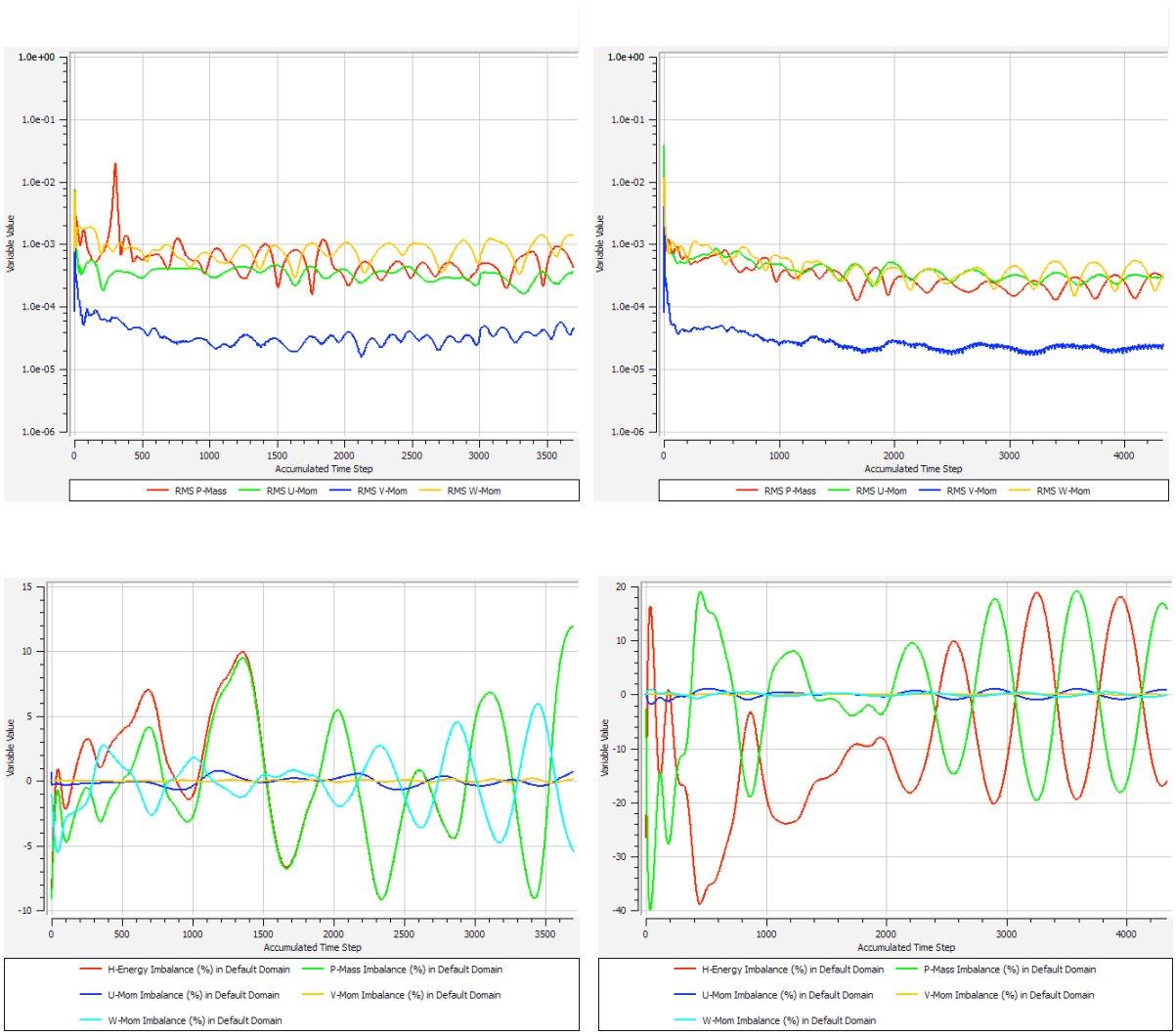

Figure 6.14: Residual and variables imbalance monitor for different FAN face boundary conditions: imposed average mass flow (left), imposed constant pressure (right).

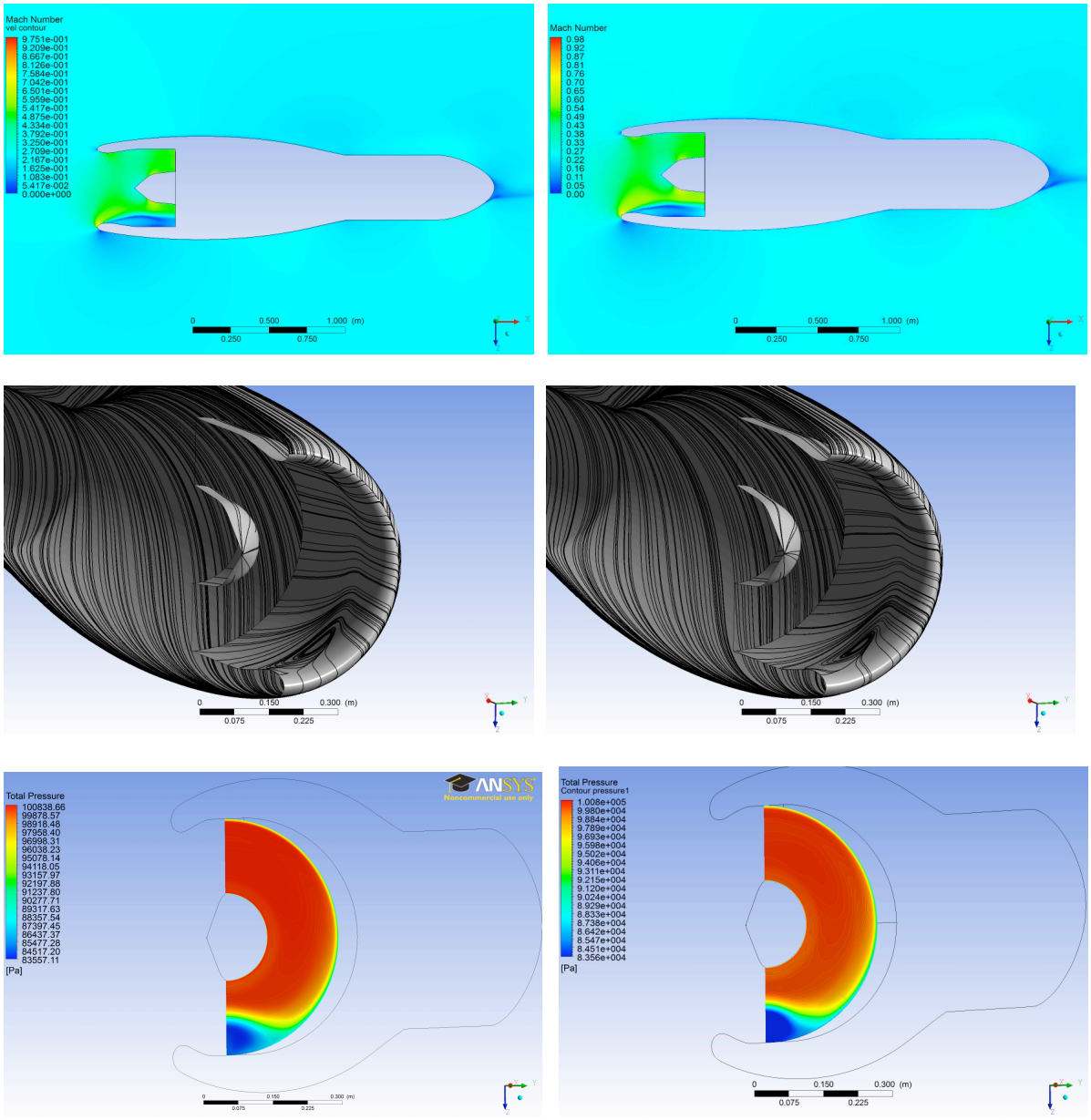

Figure 6.15: Mach number and skin-friction lines for different FAN face boundary conditions: imposed average mass flow (rigth), imposed constant pressure (left).

6.3.2 Influence of the position of the surface simulating the fan

The effect on the distortion possibly caused by the FAN face position is investigated. We have studied three geometry which differ in the distance between the virtual rotor plane and the effective FAN surface. For every simulation we have imposed a constant average static pressure of 83960 Pa on the FAN boundary. Figure 6.17 represents the contours of Mach number and the skin-friction lines for the three configurations. The flow patterns is practically the same for all the tested models. Mach number distribution is not influenced by the position of the FAN face. Even the separation seems to be not modified by different inlet lengths. The small changes we can see in the skin-friction lines are caused by the oscillating nature of the solution, according to the convergence monitor (figure 6.16), also the different starting points of the streamlines used for our visualization influence this differences. Figure 6.18 shows the total pressure contours, as we already state for the previous properties also the distortion is not influenced by the FAN position. Finally we present the y^+contours in figure 6.19. The higher y^+ value is 55 which can be considered acceptable, in addiction it reach elevated values over a small region of the nacelle.

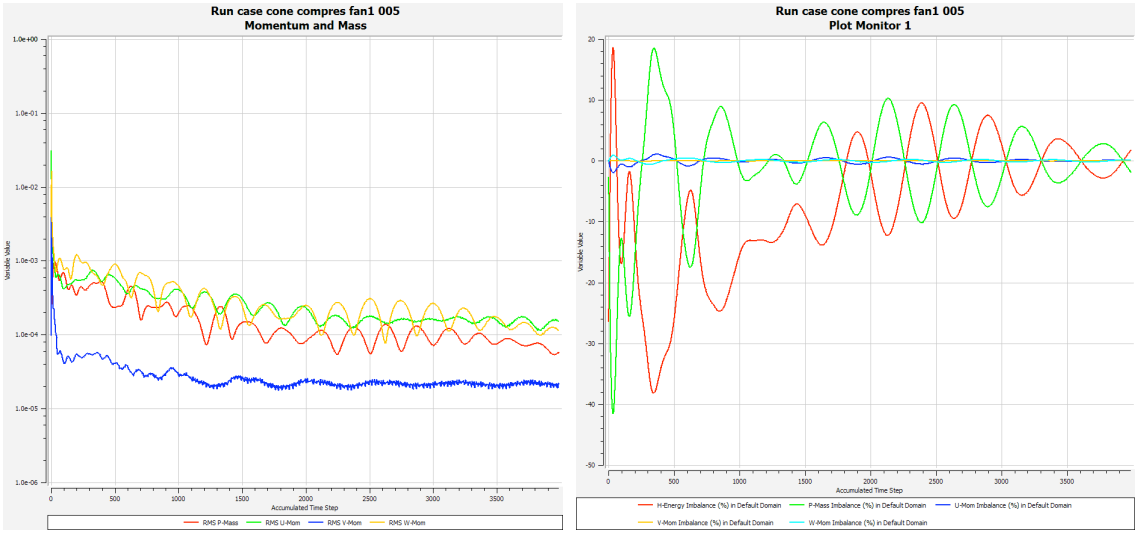

Figure 6.16: Residual and variables imbalance monitor

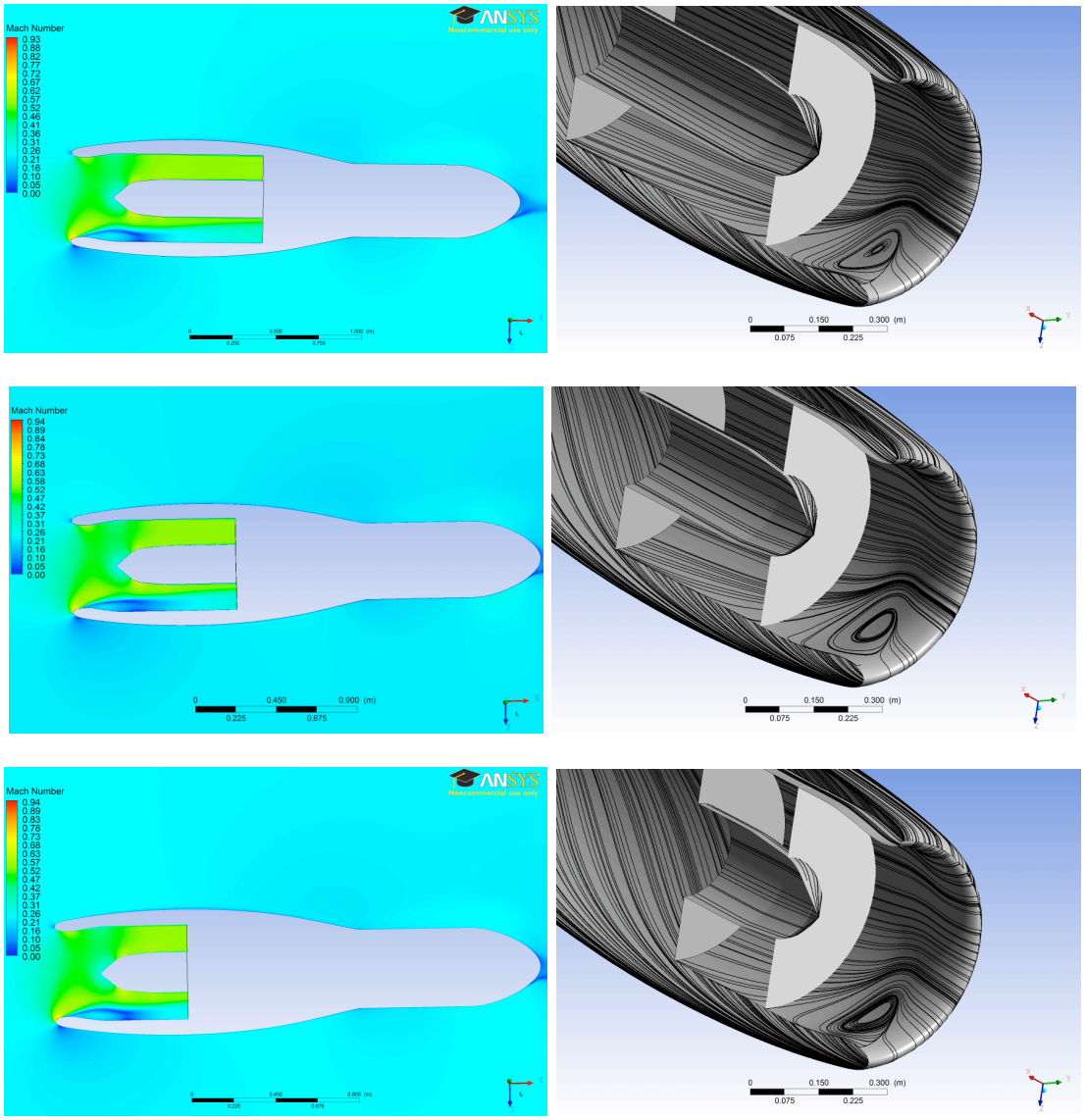

Figure 6.17: Mach number and skin-friction lines for different inlet lengths

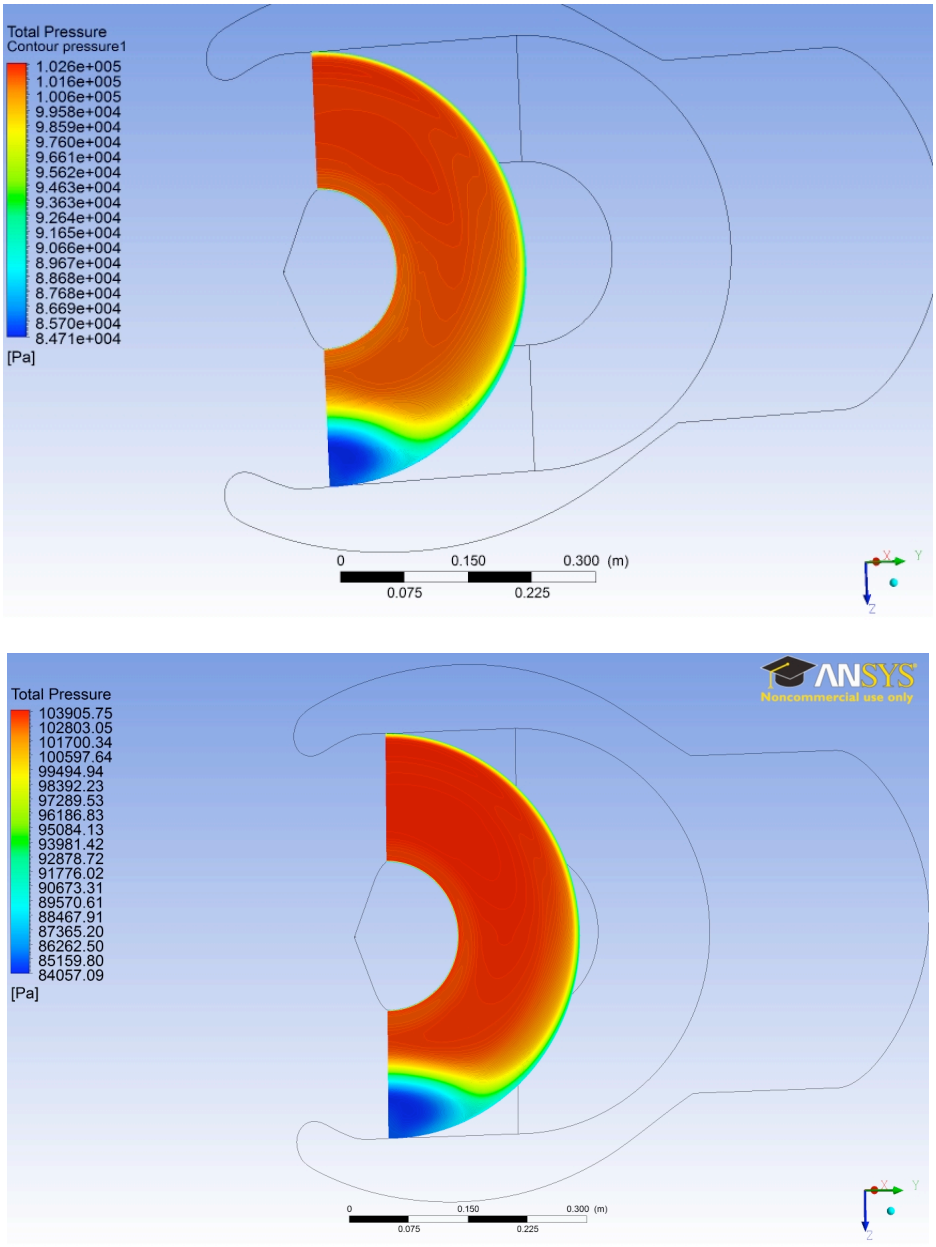

Figure 6.18: Ptot contours for different inlet lengths

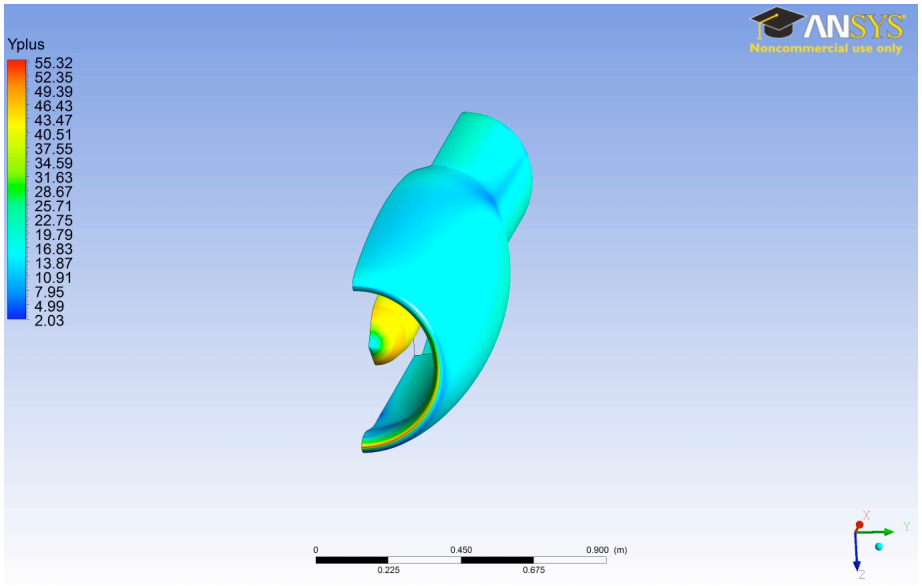

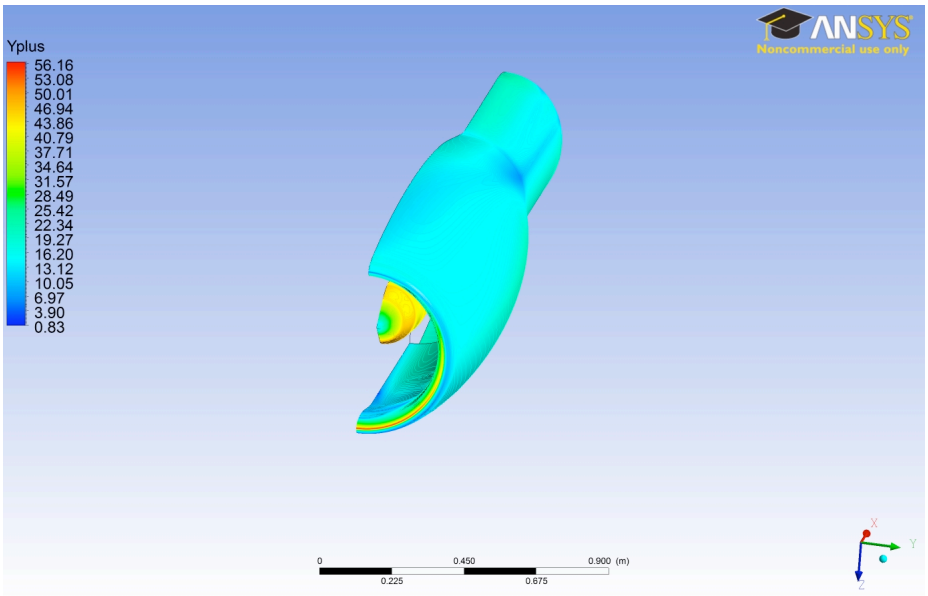

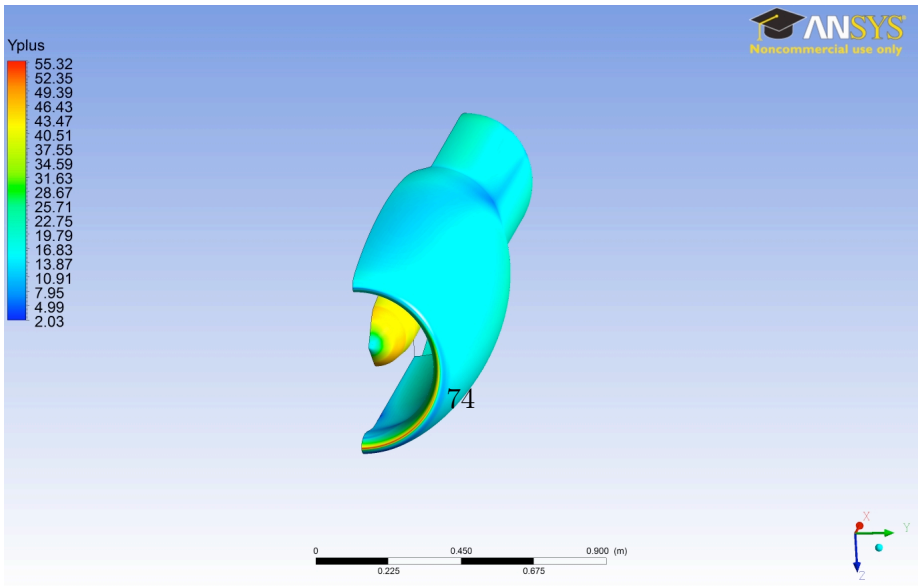

Figure 6.19: Yplus contours for different inlet lengths

Chapter 7

Conclusions and furure work

7.1 Conclusions

An introduction to the procedure employed to perform a CFD simulation has been presented. Each step of the process, from the geometric definition of the model to the numerical simulation and results analysis passing through the grid generation had been described. We have shown the fundamental phases needed for developing a multi block structured hexahedral mesh with ICEM, underling the importance of grid quality inquiry added to an iterative procedure of blocking and meshing in order to obtain satisfactory solutions. The commercial solver CFX has been tested to solve incompressible and compressible viscous steady flow around a modeled nacelle with open inlet. We have analyzed possible boundary conditions definition and different geometric configurations. At high angle of incidence the flow approaching the nacelle lip decelerates until the stagnation point and then accelerates inside the inlet. The flow detaches under the effect of strong pressure gradient and far inside the nacelle it reattaches generating a separation bubble. This phenomenon generate a heterogeneous total pressure distribution, called distortion, on the virtual plane representing the rotor. For incompressible simulations we tested the influence of the mass flow on the separation dimension. For an empty nacelle with no imposed mass flow the separation is extremely large and it almost covers the whole internal bottom side. After adding an internal boundary face simulating the engine mass flow we have certify that as the mass flow increases, the separation extent tends to reduce. Different configurations for covering nose and rear geometry has been run. The better configuration in term of convergence and plausibility of the solution is composed by a conical nose and a solid extension attached behind the nacelle which simulate the engine jet. With our final geometry compressible simulations have been performed. Two boundary conditions for the FAN face have been

studied: an imposed outgoing mass flow (as for the incompressible case) and a constant average outlet pressure. The former method has a worst and oscillating convergence but also the pressure condition case maintains an unstable oscillatory behavior even if the convergence is more rapid and obtains lower residual values. Probably for both two cases the fan surface has been posed not enough far from the separation. In fact the turbulent and unstable nature of this phenomenon does not allow a good convergence. Finally we have investigated the effect of the fan surface position on the distortion. If the boundary condition is not imposed inside or close enough the separation zone the distortion is minimally influenced by the simulating FAN face.

7.2 Future investigations

Validation of the entire meshing and solution process is needed with the comparison to experimental data. In this sense, a deeply studied nacelle with wide literature informations should be employed. We should also test different turbulence models, such as Spalart-Allmaras model. In order to improve the accuracy of the solution we should run unsteady simulations on the full annulus. In fact even if we are investigating a far field symmetric flow with no transversal velocity components once the separation occurs the solution becomes fully 3-D and unstable. In the future we should model a well-known rotor as the NASA Rotor67 with TURBOGRID, a complementary meshing tool of CFX specific for turbomachinery problem, and perform dynamic unsteady simulations with the rotating fan.

Bibliography

[1] H. K. Versteeg and W Malalasekera, "An Introduction to Computational Fluid Dynamics,The Finite Volume Method" Longman, 1995.

[2] M. B. Abbott and D. R. Basco, "Computational fluid dynamics: An introduction for engineers", Longman Scientific & Technical, 1989.

[3] A. J. Keane, P. B. Nair, "Computational approaches for aerospace design: the pursuit of excellence", Wiley, 2005

[4] C. T. Shaw, "Using Computational Fluid Dynamics" , Prentice Hall, 1992.

[5] S. V. Patankar, "Numerical Heat Transfer and Fluid Flow ", Taylor & Francis, 1980.

[6] G. F. C. Rogers, Y. R. Mayhew,"Engineering Thermodynamics: Work and Heat Transfer", Longman, 1996.

[7] Bernard Massey,"Mechanics of Fluids", Spon Press, 1998.

[8] F. M. White, "Viscous Fluid Flow", McGraw Hill, 2005.

[9] Milton, Van Dyke, "An Album of Fluid Motion" ,The Parabolic Press, 1982.

[10] L. G. Trapp, H. G. Argentieri, "Evaluation of nacelle drag using Computational Fluid Dynamics" Journal of Aerospace Technology and Management, Vol.2; No.2; pp. 145-152, 2010.

[11] Menter, F. R. , "Two-Equation Eddy-Viscosity Turbulence Models for Engineering Applications", AIAA Journal, Vol. 32, No. 8, pp. 1598– 1605, 1994.

[12] Y. Colin, B. Aupoix, J.F. Boussuge and P. Chanez, "Numerical Simulation and Analysis of Crosswind Inlet Flows at Low Mach numbers" , Proceedings of the 8th International Symposium on Experimental and Computational Aerothermodynamics of Internal Flows Lyon, July 2007

[13] C. Bommaraju, W. Ackermann, Weiland ”Finite Volume Time Domain Method On TET & HEX Meshes” Computational Electromagnetics in Time-Domain, 2007.

[14] A. Arnone, ”Viscous Analysis of Three-Dimensional Rotor Flows Using a Multigrid Method”, NASA Technical Memorandum 106266 , 1993.

[15] B.S. Seidel, “Asymmetric inlet flow in axial turbomachines”, ASME Journal of Engineering for Power, pp. 1828. 1964,

[16] F. Ehrich, “Circumferential inlet distortions in axial flow turbomachinery”, Journal of the Aeronauti cal Sciences, pp. 413417. 1957

[17] V. Jerez Fidalgo, C. A. Hall, Y. Colin, ”A study of fan distortion interaction within the NASA ROTOR67 transonic stage” , Proceedings of ASME Turbo Expo 2010: Power for Land, Sea and Air, Glasgow, 2010.

[18] D.N. Kenwright, C. Henze, C. Levit, ”Feature extraction of separation and attachment lines”, IEEE Transactions on Visualization and Computer Graphics, Vol. 5, No. 2, pp. 135-144, 1999.

[19] ”ANSYS CFX Guide”, 2010

[20] ’ANSYS ICEM CFD Guide”, 2010